Title	Numerical analyses of coupled thermal-hydraulic-mechanical-chemical processes for estimating permeability change in fractured rock induced by alkaline solution
Author(s)	Ogata, Sho; Yasuhara, Hideaki; Kinoshita, Naoki et al.
Citation	Geomechanics for Energy and the Environment. 2022, 31, p. 100372
Version Type	AM
URL	https://hdl.handle.net/11094/92441
rights	© 2022. This manuscript version is made available under the CC-BY-NC-ND 4.0 license https://creativecommons.org/licenses/by-nc-nd/4.0/
Note	

Numerical analyses of coupled thermal-hydraulic-mechanical-chemical processes for estimating permeability change in fractured rock induced by alkaline solution

Sho Ogata*, Osaka University, Suita, 565-0871, JAPAN
Hideaki Yasuhara, Ehime University, Matsuyama, 790-8577, JAPAN
Naoki Kinoshita, Ehime University, Matsuyama, 790-8577, JAPAN
Toru Inui, Osaka University, Suita, 565-0871, JAPAN
Eita Nishira, Osaka University, Suita, 565-0871, JAPAN
Kiyoshi Kishida, Kyoto University, Kyoto, 615-8530, JAPAN

*Corresponding author, E-mail address: ogata@civil.eng-osaka-u.ac.jp

Abstract

The chemical condition of groundwater, such as the pH, affects the rate of the mineral-groundwater reactions which may alter the permeability of rock masses with time. A numerical model that can address the permeability evolution of rock masses, containing newly generated fractures due to geochemical processes depending on the pH, is proposed by upgrading our coupled THMC model, *IPSACC*. Subsequently, the proposed model is utilized to estimate the long-term permeability evolution of a natural barrier composed of granite within a geological repository under subsurface conditions, considering the inflow of the alkaline cement solution from an artificial barrier which is virtually installed in a disposal cavity of HLW. In particular, a quantitative evaluation of the impact of the inflow of the alkaline cement solution on the change in permeability in the fractured rock is the novelty of this work. The computed predictions show that the fractures generated during the cavity excavation drastically increase the rock permeability near the cavity and that the rapid permeability reduction within the several shear-induced fractures is the result of the pressure solution at the contacting asperities of the fractures after the disposal of the radioactive waste into the disposal cavity. The reduction of the fracture permeability is enhanced by the increase in the pressure solution rate due to the expansion of the alkaline solution only close to the disposal cavity, while there was no enhancement in the fractures, except for close to the disposal cavity, because the alkaline solution cannot reach the fractures before the pressure solution reaches the equilibrium state within an early period after the disposal of the HLW. From these results, in the geological environment assumed in this study, it is expected that the performance of a natural barrier for delaying the migration of radionuclides over the long duration may be almost unaffected by the inflow of the alkaline solution from an artificial barrier because its impact on the permeability evolution of a natural barrier is spatiotemporally limited.

Key words: Coupled THMC numerical model, Permeability of fractured rock, Pressure solution, pH of groundwater, Fracture initiation/propagation, Inflow of alkaline solution

1 Introduction

When discussing the stability of geological repositories containing high-level radioactive waste (HLW), the long-term evolution of the hydraulic behavior of a rock mass that works as a natural barrier to the transport of radionuclides must be numerically predicted [1]. The hydraulic behavior within the natural barrier may be governed by the permeability of the multiple fractures that are generated when the cavity is excavated for the disposal of the HLW [2-8]. In addition, after the disposal of the HLW into the excavated cavity, the permeability of the fractures will be influenced by the coupled processes of various physical/chemical phenomena. These processes include the heat transfer from the waste package, the groundwater flow, and the reactive transport with geochemical reactions between the rock minerals and the groundwater (e.g., dissolution/precipitation of the rock minerals) [9, 10]. Therefore, for evaluating the long-term performance of a natural barrier, a coupled numerical model that can comprehensively explain the coupled Thermal-Hydraulic-Mechanical-Chemical (THMC) processes within fractured rock is required. In particular, among the coupled processes, the geochemical reactions between the minerals and the groundwater, such as the pressure solution at the contacting asperities and the free-face dissolution/precipitation at the free surface within rock fractures, have a non-negligible impact on the alteration of the fracture geometry/permeability over the long duration [11-21]. Several studies [13-15] have confirmed that the pressure solution at the contacting asperities within fractures may bring about the permeability evolution of the fractured rock by several orders of magnitude over a long period. As these geochemical reactions depend on the temperature, stress, and chemical conditions of the groundwater (e.g., solute concentration and pH value) [11-21], they might be affected by the inflow of the alkaline cement solution from an artificial barrier, which can be expected in the actual environments where HLW is isolated [1]. Regarding the various minerals, it was experimentally confirmed that their dissolution rate constants which control the time-dependent reaction progress of mineral dissolution significantly change depending on the pH values [21-24]. For instance, the transition of pH values from neutral to alkaline often increases the mineral dissolution rate constants [21-24]. So, the permeability evolution of rock fractures within a natural barrier due to reactions related to mineral dissolution rate constants (e.g., pressure solution and free-face dissolution/precipitation) should be altered by the inflow of the alkaline cement solution. However, although many numerical works employing coupled models have been performed [25-38], the impact of the inflow of the alkaline cement solution on the chemically induced change in the permeability of the rock fractures initiated/propagated during the cavity excavation has not yet been quantitatively evaluated.

For example, Taron et al. [37] and Renchao et al. [38] presented coupled THMC numerical simulations considering the dissolution/precipitation of multi-minerals depending on the temperature, stress, and chemical conditions of the fluid. However, their simulations can only describe the changes in permeability in the existing rock fractures because no consideration was given to the process of fracture generation. Meanwhile, although Liu et al. [39] proposed a coupled THMC numerical analysis considering the evolution of rock damage and permeability, caused by hydraulic-chemical erosion and depending on the pH values, the pressure solution was not incorporated into the analysis. Ogata et al. [40] predicted a series of rock permeability evolution processes in a natural barrier within a geological repository of HLW, from fracture generation to subsequent sealing, which results from the pressure solution and free-face precipitation by using a developed coupled THMC numerical model, denoted as the interfaces packaging problem-solving algorithm under coupled conditions, *IPSACC*. However, this numerical prediction does not consider the inflow of the alkaline cement solution from an artificial barrier because the influence of the pH values of the groundwater on the geochemical reactions is not incorporated into the model. Besides, the model does not take into account the geochemical reactions within the rock matrix, which is also necessary for precisely addressing the geochemical processes in fractured rock.

In this study, our coupled THMC numerical model, *IPSACC*, which is improved by adding the pH dependence and reaction scheme within the rock matrix to the geochemical processes, was applied to predict the long-term permeability alteration of a natural barrier composed of crystalline rocks within a repository of HLW under subsurface conditions, including the inflow of the alkaline cement solution from an artificial barrier. Performing a numerical investigation of the impact of the inflow of the alkaline cement solution on the chemically induced change in permeability of the fractured rock is the novelty of this work.

2 Numerical model

2.1 Model description

The coupled THMC numerical model, introduced in this study, is capable of addressing the interactions of numerous physical/chemical phenomena, such as the heat transfer from the waste package, the fluid flow, the fracture initiation/propagation within the rocks, solute transport, and the dissolution/precipitation of the multi-minerals in the pore fluid. A natural barrier composed of crystalline rock is the target of the numerical simulation for this model, while the phenomena in the artificial barrier are not considered. In the model, the interactions between the T, H, M, D, and C components were taken into account, as illustrated in **Fig. 1**. It should be noted that this model was established based on our previous model [40]. To date, the validation of major components of our model [40] have been examined. For instance, the evolution process in permeability/solute transport behavior due to geochemical reactions within rock fractures and the rock fracture initiation/growth process described by damage theory, were validated by comparing with the flow-through experiments using single rock fractures conducted under coupled THMC conditions [30] and the mechanical test including the brittle failure process of a rock specimen [41], respectively.

In present study, our model [40] was further upgraded by making some improvements. The most important improvement was to expand the model and its realm of implementation for computing the laws of geochemical reactions depending on the pH distribution in the fractured rock. This improvement will enable consideration of the influence of the inflow of the alkaline cement solution from an artificial barrier, and will be helpful for analyzing and understanding the controlling factors for the long-term permeability evolution of fractured rock under the expected environment of geological repositories of HLW. The other major improvement was to add consideration of the geochemical reactions in the rock matrix, while the previous model [40] considered only the reactions in the rock fractures. The above-mentioned improvements are expressed in blue letters in **Fig. 1**.

2.2 Governing equations

The coupled THMC processes addressed in the proposed model are computed using some governing equations, including Darcy's law and the conservation law of water mass, the heat transfer equation, the poroelastic theory, the scalar damage model, the solute transport equation, and the law of mineral dissolution/precipitation. In this section, these governing equations are introduced in order.

2.2.1 Mechanical equilibrium

The target material for the model is assumed as a saturated crystalline rock, indicating the behavior of an elastic body. Regarding the mechanical behavior, and assuming the plane strain condition, the stress/deformation distributions in the rock mass are evaluated by the quasi-static equilibrium equation and the typical Hooke's law, including the effect of the pore pressure and thermal expansion based on the poroelastic theory, as follows:

$$-\nabla \cdot \boldsymbol{\sigma} = \boldsymbol{F}_v \tag{1}$$

$$\boldsymbol{\sigma} = C : (\boldsymbol{\varepsilon} - \boldsymbol{\alpha}_T \Delta T) + \alpha_B p \boldsymbol{I} \tag{2}$$

where $\boldsymbol{\sigma}$ [Pa] is the stress tensor, $\boldsymbol{F_v}$ [Pa m^{-1}] is the body force, $\boldsymbol{C}$ [Pa] is the elasticity tensor, p [Pa] is the pore pressure, $\boldsymbol{\varepsilon}$ [-] is the strain tensor, $\boldsymbol{\alpha_T}$ [K^{-1}] is the thermal expansion coefficient of the solid, T [K] is the temperature, α_B [-] is the Biot-Willis coefficient, and $\boldsymbol{I}$ [-] is the identity tensor.

2.2.2 Damage evolution

The initiation and propagation of rock fractures within a rock mass are computed by the isotropic scalar damage model which has been applied in a lot of simulations for fracture evolution [31-33, 42-48]. In the current model, the behavior of the damage evolution is expressed by a formulation proposed previously by Tang (1997) [42] and Zhu and Tang (2004) [44]. As depicted in **Fig. 2,** the elastic damage constitutive law for an element under the conditions of uniaxial tension and uniaxial compression is utilized to simulate the rock fracturing process. It is noted that the tensile stress and the compressive stress are set to be negative stress and positive stress, respectively. Damage in tension or in shear begins to progress when the stress state of an element reaches the maximum tensile stress criterion or the Mohr-Coulomb failure criterion, respectively, given by

$$\begin{cases} F_t \equiv -\sigma'_3 - f_{t0} = 0 \\ F_s \equiv \sigma'_1 - \dfrac{1+\sin\theta}{1-\sin\theta}\sigma'_3 - f_{c0} = 0 \end{cases} \tag{3}$$

where F_t and F_s are the two damage threshold functions for tensile damage and shear damage, respectively, σ'_1 ($= \sigma_1 - \alpha_B p$) [Pa] and σ'_3 ($= \sigma_3 - \alpha_B p$) [Pa] are the maximum and minimum effective principal stresses, respectively, f_{t0} [Pa] and f_{c0} [Pa] are the uniaxial tensile strength and uniaxial compressive strength, respectively, and θ [°] is the internal friction angle.

In the isotropic damage theory, the elastic modulus E of the damaged rock monotonically decreases with the progress of the damage, as follows:

$$E = (1-\omega)E_0 \tag{4}$$

where E_0 [Pa] and E [Pa] are the elastic moduli of the rock before and after the initiation of damage, respectively, and ω [-] is the scalar damage variable that changes from 0 to 1.0 and expresses the degree of damage to the targeted material. ω becomes 0 when no damage occurs and 1 when complete damage occurs. In the current work, the zone where damage has progressed considerably ($\omega > \omega_{cr} = 0.8$) is treated as a mesoscopic fracture. And, this mesoscopic fracture (damage zone: $\omega > \omega_{cr}$) is defined as a “fracture”, while a macroscopic fracture, composed of the calescence of multiple mesoscopic fractures, is generally called a fracture. Meanwhile, the zone where $\omega \le \omega_{cr}$ is treated as the rock matrix zone. Damage variable ω is computed by strain, as follows [45].

According to the failure criteria of Eq. (3) and the constitutive relationship shown in **Fig. 2**, damage variable ω is computed as follows:

$$\omega = \begin{cases} 0 & F_t < 0 \text{ and } F_s < 0 \\ 1 - \dfrac{\eta \varepsilon_{t0}}{\varepsilon_t} & F_t = 0 \quad \text{and} \quad \Delta F_t > 0 \\ 1 - \dfrac{\eta \varepsilon_{c0}}{\varepsilon_c} & F_s = 0 \quad \text{and} \quad \Delta F_s > 0 \end{cases} \tag{5}$$

$$\varepsilon_t = \frac{1}{1+v}\left[\varepsilon_3 + \frac{v}{1-2v}\varepsilon_v\right] \tag{6}$$

$$\varepsilon_c = \frac{1}{1+v}\left[\varepsilon_1 + \frac{v}{1-2v}\varepsilon_v\right] - \frac{1+\sin\theta}{1-\sin\theta}\frac{1}{1+v}\left[\varepsilon_3 + \frac{v}{1-2v}\varepsilon_v\right] \tag{7}$$

where ε_{t0} [-] and ε_{c0} [-] are the limit tensile strain and compressive strain, respectively, η [-] is a constant ($\eta = 0.1$), ε_i (i = 1, 2, 3) are the principle strains in the first, second, and third principal stress directions, respectively, ε_v [-] is the volumetric strain, and v [-] is Poisson's ratio.

2.2.3 Characterization of heterogeneity

The heterogeneity of the rock mass is considered by setting the mechanical properties of each element in the calculation domain according to the Weibull distribution, as defined in the following probability density function [49]. Specifically, among the mechanical properties, the heterogeneity is considered in setting the elastic modulus, uniaxial tensile strength, and uniaxial compressive strength [42, 44].

$$f(u)=\frac{m}{u^{s}}\left(\frac{u}{u^{s}}\right)^{m-1}\exp\left[-\left(\frac{u}{u^{s}}\right)^{m}\right] \tag{8}$$

where u is the mechanical parameter of each element in the calculation domain, such as the strength and the elastic modulus (i.e., $u = E_0, f_{t0}$, and f_{c0}), u^{s} is the characteristic parameter which is related to the average value of that mechanical parameter (i.e., $u^{s} = E_0^{s},\ f_{t0}^{\ s},$ and $f_{c0}^{\ s}$), and m [-] is the homogeneity index of the material properties which defines the shape of the distribution function.

The behavior of the groundwater flow within a rock mass is described by the conservation of water mass employing poroelasticity and by assuming the Darcian flow as

$$\rho_w S\frac{\partial p}{\partial t}+\nabla\cdot(\rho_w \boldsymbol{u})+\rho_w \alpha_B\frac{\partial \varepsilon_v}{\partial t}=f_w \tag{9}$$

$$\boldsymbol{u}=-\frac{\boldsymbol{k}}{\mu}(\nabla p+\rho_w g\nabla h) \tag{10}$$

$$S=\frac{\varphi}{K_f}+\frac{(1-\varphi)}{K_s} \tag{11}$$

$$\alpha_B=1-\frac{K}{K_s} \tag{12}$$

where ρ_w [kg m^{-3}] is the liquid density, S [Pa^{-1}] is the storage coefficient, $\boldsymbol{u}$ [m s^{-1}] is the liquid velocity tensor, f_w [kg m^{-3} s^{-1}] is the source term for the flow, $\boldsymbol{k}$ [m^{2}] is the rock permeability tensor, μ [Pa s] is the liquid dynamic viscosity, g [m s^{-2}] is the gravity acceleration, and h [m] is the potential head, φ

is the porosity at an arbitrary time, K [Pa] is the bulk modulus of the rock, K_f [Pa]is the bulk modulus of the fluid, and K_s [Pa] is the bulk modulus of the solid. The permeability within the rock mass is distinguished by the degree of damage [50], namely,

$$k = \begin{cases} k_0 \dfrac{(1-\varphi_i)^2}{(1-\varphi)^2} \left(\dfrac{\varphi}{\varphi_i} \right)^3 \exp(\alpha_k \omega) & \omega \le \omega_{cr} \\ \dfrac{b_f^{\,2}}{12} & \omega > \omega_{cr} \end{cases} \tag{13}$$

where k_0 [m^2] is the permeability of the undamaged rock, φ_i is the initial porosity, α_k [-] is the damage-permeability effect coefficient, and b_f [m] is the average fracture aperture which is defined only in the damage zone where $\omega > \omega_{cr}$. As shown in Eq. (13), the change in permeability of the rock matrix, due to the change in porosity, is considered by applying the Kozeny-Carman equation [51], while it was not considered in our previous model [40]. The occurrence of a fracture aperture brought about the damage progression, $b_{f,\omega}$, is expressed as [50]

$$b_{f,\omega} = \sqrt{12 k_0 \exp(\alpha_k \omega)} \tag{14}$$

2.2.4 Heat transfer

In the thermal transport process, the temperature field within the rock is determined by solving the following heat transfer equations:

$$(\rho C_p)_{eq} \frac{\partial T}{\partial t} = \nabla \cdot (\boldsymbol{\lambda_{eq}} \nabla T) - \rho_w C_{p,w} \boldsymbol{u} \cdot \nabla T + q_h \tag{15}$$

$$(\rho C_p)_{eq} = (1-\varphi)\, \rho_m C_{p,m} + \varphi\, \rho_w C_{p,w} \tag{16}$$

$$\boldsymbol{\lambda}_{eq} = (1-\varphi)\,\boldsymbol{\lambda}_{m} + \varphi\,\boldsymbol{\lambda}_{w} \tag{17}$$

where $(\rho\, C_p)_{eq}$ [J K^{-1} m^{-3}] is the equilibrium volumetric heat capacity, $C_{p,w}$ [J kg^{-1} K^{-1}] is the heat capacity of the fluid, $\boldsymbol{\lambda}_{eq}$ [W m^{-1} K^{-1}] is the equilibrium thermal conductivity tensor, q_h [W m^{-3}] is the heat source, ρ_m [kg m^{-3}] is the density of the solid, $C_{p,m}$ [J kg^{-1} K^{-1}] is the heat capacity of the solid, and $\boldsymbol{\lambda}_m$ and $\boldsymbol{\lambda}_w$ [W m^{-1} K^{-1}] are the thermal conductivity tensors of the solid and the liquid, respectively.

The thermal conductivity is correlated according to the evolution of damage [33] as

$$\lambda_m = \lambda_{m0} \exp(\alpha_\lambda\, \omega) \tag{18}$$

where α_λ [-] is the damage-solid thermal conductivity coefficient, and λ_{m0} [W m^{-1} K^{-1}] is the initial thermal conductivity of the solid without damage.

2.2.5 Reactive transport

The advection-diffusion equation, including the reaction term, is utilized to describe the distribution of solute concentrations. The mechanical dispersion and retardation, brought about by the sorption processes, are not taken into account here.

$$\frac{\partial(c_i\varphi)}{\partial t} + \boldsymbol{u}\cdot\nabla c_i = \nabla\cdot(\boldsymbol{D}_{e,i}\nabla c_i) + \textstyle\sum_j^n \upsilon_i r_j \tag{19}$$

$$\boldsymbol{D}_{e,i} = \varphi\tau\, \boldsymbol{D}_{b,i} \tag{20}$$

where c_i [mol m^{-3}] is the concentration of solute i, $\boldsymbol{D}_{e,i}$ [m^2 s^{-1}] is the effective diffusion coefficient tensor, $\boldsymbol{D}_{b,i}$ [m^2 s^{-1}] is the diffusion coefficient tensor, τ [-] is the coefficient related to tortuosity (τ = 1.0), υ_i [-] is the stoichiometry coefficient of solute i, n is the number of rock-forming minerals, and r_j [mol m^{-3} s^{-1}] is the rate of geochemical reactions for mineral j. $\sum_j^n \upsilon_i r_j$ represents the supply of solute concentration due to geochemical reactions of rock-forming minerals. The dissolution rate constant and diffusion coefficient are controlled by the system temperature and can be defined by an Arrhenius-type equation [52].

$$D_{b,i} = D_{b,i}^{0} \exp(-E_{D,i}/RT) \tag{21}$$

where $D_{b,i}^{0}$ [m^2 s^{-1}] and $E_{D,i}$ [J mol $^{-1}$] are the pre-exponential factor and the activation energy of the diffusion of solute i, respectively, and R [J mol $^{-1}$K^{-1}] is the gas constant.

2.2.6 Geochemical reactions

The geochemical reactions between rock and water include the free-face dissolution/precipitation and the pressure solution. Therefore, the rate of the geochemical reactions for mineral j, r_j, is represented as

$$r_j = r_j^{FF} + r_j^{PS} \tag{22}$$

where r_j^{FF} [mol m^{-3} s^{-1}] is the rate of the free-face dissolution/precipitation of mineral j within the rock, and r_j^{PS} [mol m^{-3} s^{-1}] is the rate of the pressure solution of mineral j within the rock.

In the current model, geochemical reactions within both fracture and matrix domains are considered. However, based on the equations of the pressure solution law, presented in Yasuhara et al. (2016)[36], it can be inferred that the pressure solution at the grain contacts within the matrix domain may not occur in crystalline rock that has extremely low porosity. Thus, among the reactions within the matrix domain, only free-face dissolution/precipitation is considered, while the pressure solution is not considered. The equation for the rate of the reactions within the fracture is formulated by setting the geometric model derived by idealizing the arbitrary micro-domain as the representative element of the fracture area (**Fig. 3** [13]). In the proposed model, the greatly damaged zone, where $\omega > \omega_{cr}$, is defined as the fracture, while the other zone is assumed as the rock matrix. Consequently, the rates of the free-face dissolution/precipitation in the matrix and fracture domains can be defined by using the damage variable in the following equation. The equations for the matrix and fracture domains are given in Lasaga (1984) [53] and Ogata et al. (2018) [30], respectively.

$$\begin{cases} r_j^{FF} = f_r \chi_j k_{+,j} A_{geo}(1 - Q_j / K_{eq,j}) & \omega \leq \omega_{cr} \\ r_j^{FF} = 2 f_r \chi_j k_{+,j}(1 - Q_j / K_{eq,j}) / b_f & \omega > \omega_{cr} \end{cases} \tag{23}$$

where $k_{+,j}$ [mol m^{-2} s^{-1}] is the mineral dissolution rate constant of mineral j, χ_j [-] is the volumetric ratio of mineral j, f_r [-] is the roughness factor, which is the ratio of the true (microscopic) surface area over the apparent (geometric) surface area, Q_j [-] is the ionic activity product, $K_{eq,j}$ [-] is the equilibrium constant of mineral j, and A_{geo} [m^2 m^{-3}] is the geometric surface area, which is simply evaluated by the ratio of the surface area of the spherical grain of diameter d over the volume, as follows:

$$A_{geo} = \frac{\pi d^2}{\frac{\pi d^3}{6}} = \frac{6}{d} \tag{24}$$

The rate of the pressure solution for mineral j at the contacting asperities within the fracture is expressed by applying the damage variables, criterions for tension and shear damage, given as [40]

$$\begin{cases} r_j^{PS} = 0 & \omega \le \omega_{cr} \\ r_j^{PS} = \dfrac{3R_c f_r \chi_j V_{m,j} k_{+,j}}{RT b_f (1-R_{f,c})} \left\langle \dfrac{\langle \sigma'_3 \rangle}{R_{f,c}} - \sigma_c \right\rangle & \omega > \omega_{cr} \quad \text{and} \quad F_t = 0 \\ r_j^{PS} = \dfrac{3R_c f_r \chi_j V_{m,j} k_{+,j}}{RT b_f (1-R_{f,c})} \left\langle \dfrac{\langle \sigma'_1 \rangle + \langle \sigma'_3 \rangle}{R_{f,c}} - \sigma_c \right\rangle & \omega > \omega_{cr} \quad \text{and} \quad F_s = 0 \end{cases} \tag{25}$$

where R_c [-] is the contact-area ratio within the fracture, $V_{m,j}$ [m^3 mol^{-1}] is the molar volume of mineral j, σ_c [pa] is the critical stress, and <> are the Macaulay's brackets. According to Eq. (25), the pressure solution induced by compressive stress does not occur within the tension fracture when $\sigma_3 < 0$, but it can occur when the stress state moves to a compressive state (i.e., $\sigma_3 > 0$).

The mineral dissolution rate constants, that are significantly important parameters for realizing the geochemical reaction between the rock-forming minerals and water, are represented by the Arrhenius expression with dependence on temperature and the pH condition (i.e., concentration of H^+ in the pore water), given as [21]

$$k_{+,j} = k_{1,j} a_{H^+}^{\,n1} + k_{2,j} + k_{3,j} a_{H^+}^{\,n3}, \tag{26}$$

$$k_{i,j} = k_{i,j}^{298.15K} \exp\left[\frac{-E_{i,j}}{R} \left(\frac{1}{T} - \frac{1}{298.15K} \right) \right], \tag{27}$$

where $k_{i,j}^{298.15K}$ (i = 1, 2, 3) [mol m^{-2} s^{-1}] is the rate constant of mineral j at 298 1.5K (25°C), pH = 0 under acid, neutral, and base mechanisms, respectively, $E_{i,j}$ (i = 1, 2, 3) [J mol^{-1}] is the activation energy of mineral j under acid, neutral, and base mechanisms, respectively, a_{H+} is the activity of H$^+$, and n_1 and n_3 are the dimensionless catalysis constants for the acid and base mechanisms, respectively. In the current work, an essential improvement is made on our previous model [40] by introducing Eq. (26) for examining the influence of the pH alterations brought about by the inflow of the alkaline cement solution from an artificial barrier on the chemically induced permeability change with time in a natural barrier.

2.2.7 Porosity change within rock matrix

The changes in both the matrix porosity and the fracture aperture are thought to be related to the structure alteration of the pore space within the rock, while the former was not considered in our previous work [40]. In the current model, the change in porosity is only induced by the geochemical effect. Thus, the porosity of the rock matrix zone ($\omega \le \omega_{cr}$) at an arbitrary time is obtained by computing the rate of change in porosity due to the free-face dissolution/precipitation within the rock matrix, as follows:

$$\varphi = \varphi_i + \int \dot{\varphi}^{FF} \, dt \,, \tag{28}$$

$$\dot{\varphi}^{FF} = \sum_j^n V_{m,j} r_j^{FF} = \sum_j^n f_r \chi_j V_{m,j} k_{+,j} A_{geo} (1 - Q_j / K_{eq,j}) \,, \tag{29}$$

where $\dot{\varphi}^{FF}$ is the rate of change in porosity of the free-face dissolution/precipitation within the rock matrix.

2.2.8 Fracture aperture change

The change in the fracture aperture stems from the fracture initiation/propagation and geochemical processes. Therefore, the aperture of the fractured zone ($\omega > \omega_{cr}$) at arbitrary time t is defined by taking account of the aperture brought about by the fracture initiation/propagation and the temporal evolution of the aperture induced by the free-face dissolution/precipitation and pressure solution, as follows:

$$b_f(t) = b_{f,\omega} + \int \dot{b}_f^{FF}(t)dt + \int \dot{b}_f^{PS}(t)dt \, , \tag{30}$$

$$\dot{b}_f^{FF} = \sum_j^n 2 f_r \chi_j (1 - R_{f,c}) V_{m,j} k_{+,j} (1 - Q_j / K_{eq,j}) \tag{31}$$

$$\begin{cases} \dot{b}_f^{PS}(t) = \sum_j^n \dfrac{-3 f_r \chi_j k_{+,j} V_{m,j}^2}{RT} \left\langle \dfrac{\langle \sigma'_3 \rangle}{R_{f,c}} - \sigma_c \right\rangle & \omega > \omega_{cr} \quad \text{and} \quad F_t = 0 \\ \dot{b}_f^{PS}(t) = \sum_j^n \dfrac{-3 f_r \chi_j k_{+,j} V_{m,j}^2}{RT} \left\langle \dfrac{\langle \sigma'_1 \rangle + \langle \sigma'_3 \rangle}{R_{f,c}} - \sigma_c \right\rangle & \omega > \omega_{cr} \quad \text{and} \quad F_s = 0 \end{cases} , \tag{32}$$

where $\dot{b}_f^{FF}$ [m s^{-1}] is the rate of change in the fracture aperture by the free-face dissolution/precipitation and $\dot{b}_f^{PS}$ [m s^{-1}] is the rate of change in the fracture aperture by the pressure solution. It may be possible to approximate the correlation between the fracture aperture and the contact-area ratio on the fractures by the following simple representation [14]:

$$b_f(t) = b_{f,r} + (b_{f,\omega} - b_{f,r}) \exp(-(R_{f,c}(t) - R_{f,c\omega}) / a) \, , \tag{33}$$

where $b_{f,r}$ [m] is the residual fracture aperture, a [-] is a constant, and $R_{f,c\omega}$ [-] is the contact-area ratio within the fracture when a fracture is generated, which is represented as the following equation based on the theoretical background for damage variable ω [54]. The detailed derivation process is explained in the literature [40].

$$R_{f,c\omega} = 1 - \omega \ . \tag{34}$$

It is noted that, in the present work, after the fracture initiation/propagation, changes in damage variable ω are not considered.

2.2.9 Numerical computing system

The proposed model is implemented into the computing system by linking two numerical tools of COMSOL MULTIPHYSICS, a powerful FEM software package [60], and PHREEQC [61], a computer program that performs various aqueous geochemical calculations. The main feature of the calculation procedure is that it solves the reactive transport process (Eq. (19)) by dividing it into two processes based on a non-iterative sequential split operator approach [62]. One process is the solute transport, which is handled in COMSOL MULTIPHYSICS, and the other process comprises the kinetic geochemical reactions, including the free-face dissolution/precipitation and the pressure solution, which is computed by PHREEQC.

Details on the above-mentioned computing system including the benchmark test for verifying the correctness of the linking between the COMSOL MULTIPHYSICS and the PHREEQC, can be found in the literature [40].

3 Numerical investigations of permeability evolution within natural barrier for geological disposal of HLW

The proposed model was applied to numerical simulations for predicting the long-term permeability alteration in rock that works as a natural barrier within a geological repository of HLW. The environment of the target subsurface in the following simulations was set by referring to the Mizunami area of Gifu, Japan, and the actual data were obtained from relevant literature. In the simulations, the horizontal storage system of radioactive waste, introduced in the scientific and technical report summarizing HLW disposal construction in Japan [1], was assumed. The numerical domain, as illustrated in **Fig. 4**, expresses the natural barrier from depths of 450 m to 550 m from the Earth's surface. The disposal cavity had a depth of 500 m and its domain was discretized into 51064 rectangular elements. The canisters of radioactive waste were virtually installed in the cavity as a heat source. The horizontal length of 13.32 m was selected for the numerical domain because it may be one-half of the center-to-center distance of each disposal cavity with a diameter of 2.22 m. The numerical domain was composed of granite with a porosity of 1.12% and a dry density of 2620 kg/m^3. These physical properties were determined by observing core samples drilled from the target site at a depth of 500 m [55]. Considering the heterogeneity of the mechanical properties in the target rock mass, the elastic modulus and strengths (uniaxial tensile strength and uniaxial compressive strength) were distributed within the domain based on the Weibull distribution, and the other properties were set homogeneously. In the current simulations, firstly, an excavation analysis of the disposal cavity was performed. Subsequently, the long-term prediction of the alteration in permeability was implemented by employing the stress condition and the damage distribution obtained from the excavation analysis as the initial conditions. The parameters used in the simulations are shown in **Table 1**. These parameter values were selected by referring to the literature [14, 31, 44, 46, 52, 55~ 59].

3.1 Numerical analysis of disposal cavity excavation

Through the numerical analysis of the disposal cavity, with a diameter of 2.22 m and a depth of 500 m, shown in **Fig. 4**, the behavior of the fracture initiation/propagation rock was predicted. The characteristic parameters related to the average value of the mechanical properties, distributed by the Weibull distribution (i.e., $f_{t0}^{\ s}$, $f_{c0}^{\ s}$, and $E_0^{\ s}$, (see Eq. (8)), were set to be 5.36 MPa, 159.6 MPa, and 50.3 GPa, respectively. These values are equivalent to the mechanical properties evaluated by the core samples collected in-situ from a depth of 500 m [55]. Employing an appropriate value for homogeneity index *m* (see Eq. (8)), in the range of 1.2~5.0, as shown in previous studies [44, 46], the value of that parameter was set to be 2.0. Poisson's ratio and the internal friction angle were set to be 0.27 and 52.6°, respectively [55]. The initial stress conditions, given in **Fig. 5**, were approximated from the data obtained from the hydraulic fracturing tests conducted at various depths at the target site, and lateral pressure coefficient K_0 was set to be 1.6704 [63]. The initial pore pressure was equivalent to the hydrostatic pressure at the steady state. In the excavation analysis, the excavated wall was set to be in an undrained condition during the excavation because a short-term excavation was assumed. To simulate the excavation process in this analysis, the internal outward radial pressure applied to the cavity boundary was reduced monotonically by 0.25 % per step for 400 steps (**Fig. 5**). The fracturing process (change in distribution of damage variable ω) around the disposal cavity during the excavation is depicted in **Fig. 6**. The figure distinguishes the tensile damage from the shear damage by modifying the sign for the damage variable ω values in the shear mode to negative (i.e., $0 \leq \omega \leq 1 \Rightarrow -1 \leq \omega \leq 0$). Thus, the negative numbers ($-1 \leq \omega < 0$) express the shear damage (areas with red color), while the positive ones express the tensile damage (areas with blue color). The figure shows that multiple fractures grow vertically around the crown, and that the invert and tensile damage is more remarkable than the shear damage. The shear damage occurs near the tensile damage. The maximum principal stress is further increased by the stress concentration due to the decrease in stiffness (reduction) in the neighboring tensile damage zone which may result in shear failure near the tensile damage.

3.2 Long-term simulations with THMC coupling

The initial conditions were set by employing the physical/chemical properties of the target rock that were updated by the damage state (i.e., elastic modulus, permeability, thermal conductivity, fracture aperture, and contact-area ratio within the fracture) through the excavation analysis. Subsequently, the long-term simulations were performed. These long-term simulations target the coupled THMC phenomena after the disposal of the waste package in the excavated cavity. The target rock was assumed to be composed of five minerals, namely, quartz (50 vol%), k-feldspar (12 vol%), albite (10 vol%), anorthite (20 vol%), and biotite (8.0 vol%). These volumetric ratios of the minerals, χ_j, were given by referring to those evaluated by the XRD analysis with Mizunami granite [14]. The important parameters of the kinetic dissolution rate constants (see Eqs. (26) and (27)) for the minerals considered in the simulations, obtained from Palandri and Kharaka (2004) [21] and Li et al. (2006) [64], are given in **Table 2**. The hydraulic and thermal gradients were set to be 0.01 and 2°C/100 m, respectively [65]. When considering radiation from canisters, time-dependent change T_b(t) outside the buffer material, obtained from the literature [1] (**Fig. 7**), was set at the periphery of the cavity as the boundary conditions. The inflow of the alkaline cement solution from an artificial barrier was virtually considered by setting solute concentration $c_{i,\mathrm{in}}$, shown in **Table 3**, at the periphery of the cavity as the boundary conditions. The solute concentrations contained in the alkaline cement solution were determined with reference to the literature [66, 67]. A summary of the boundary/initial conditions used in long-term simulations is shown in **Fig. 8**. The chemical conditions of the groundwater at the initial state, including the solute concentrations and the pH value shown in **Table 4**, were set to be the measured values at the target site at a depth of 500 m [68]. In the present work, the fracture initiation/extension is considered during the excavation process of the disposal cavity; namely, the forming of new fractures after the excavation is not taken into account.

In the present work, the long-term predictions were implemented in two different cases. The first case is that which virtually considers the inflow of the alkaline cement solution from an artificial barrier by setting the concentrations shown in **Table 3** at the cavity boundary; it is called the “inflow”. The other case is that which excludes the above-mentioned inflow phenomenon; it is called the “no-inflow”. **Fig. 8** shows the boundary/initial conditions utilized in the inflow case. In the no-inflow case, the following Neumann boundary condition is set at the cavity boundary instead of the inlet conditions used in the “inflow” case.

$$\frac{\partial c_i}{\partial \boldsymbol{n}} = 0 . \tag{35}$$

where $\boldsymbol{n}$ represents the outward normal direction to the targeted boundary.

The changes in the permeability distribution around the cavity with time in the range of 0 – 4.0 years, under the no-inflow condition and the inflow condition, are shown in **Fig. 9**. In the figure, the permeability is given by log notation (i.e., $\log_{10}k$). The initial state shown in figure suggests that the permeability in the fractured zone, formed by the cavity excavation, increases to about two orders of magnitude greater than the intact rock zone at the maximum. As shown in the figure, in both cases, the permeability within several fractures eventually decreases with time. This may be because of the geochemical reactions that seal the fracture (i.e., pressure solution and precipitation). In the figure, the maximum reduction in permeability is about two orders of magnitude and is almost complete at 0.1 years. The difference in permeability evolution between the two cases cannot be clearly confirmed with the time tracking shown in the figure. On the other hand, within the undamaged zones, the permeability around the cavity remains almost unchanged in both cases.

An additional case was computed under the inflow condition, which does not consider the occurrence of the pressure solution, in order to examine which geochemical reaction dominates the permeability reduction within the fractures. Permeability distributions at the initial state and after 1.0 years, predicted in the above-mentioned case, are shown in **Fig. 10**. The figure shows that, in the case which does not involve the pressure solution, the permeability within the fractures is almost unchanged. Thus, the decrease in fracture permeability with time, observed in **Fig. 9,** is mainly controlled by the occurrence of the pressure solution at the contacting asperities within the fractures. A comparison of **Figs. 6** and **9** implies that the fractures where the permeability changes almost coincide with the shear-induced fractures. This is because the driving force of the pressure solution is the compressive stress which does not occur under the tensile stress condition.

In order to investigate the difference in permeability evolution within the fractures, by the influence of the inflow of the alkaline solution, the changes in permeability at an early period under the no-inflow and inflow conditions are shown in **Fig. 11**. In figure, the permeability distribution, except for the rock matrix, is extracted to visualize the permeability evolution within the fractures. It should be noted that the permeability is normalized by the initial value of this long-term coupled analysis after the disposal of the waste package. The figure shows that the relatively clear difference in the permeability distribution close to the cavity at 0.001 years between the two cases can be confirmed visually, while there is almost no remarkable difference after 0.1 years. The distributions of normalized fracture permeability focused near the invert at 0.001 years under the no-inflow condition and the inflow condition are shown in **Fig. 12.** As is apparent from the figure, the progress of the permeability reduction under the inflow condition is faster than that under the no-inflow condition. In addition, to further examine the spatiotemporal extent of occurrence of difference in the permeability evolution due to the influence of the inflow of alkaline solution confirmed in **Figs. 11** and **12**, the ratio of the fracture permeability distribution under the inflow condition (k_{inflow}) and that under the no-inflow condition ($k_{\mathrm{no\text{-}inflow}}$), with time in range of 10^{-3}–0.1 years, are shown (**Fig. 13)**. In the figure, clearly colored areas indicate the locations where the clear differences occur in fracture permeability evolution between two cases (inflow condition and no-inflow condition). From the figure, it can be recognized that at 0.05 years after the disposal of the waste package, the clear differences in permeability close to the cavity between two cases have already disappeared. The maximum spatial extent where the above-mentioned permeability difference can be observed, is about 0.2 m from the cavity wall. Subsequently, the changes in pH within the fractures with time, under the no-inflow condition and the inflow condition, are presented in **Fig. 14**. In the figure, it is shown that the pH close to the cavity increases to around 12 due to the gradual expansion of the alkaline solution from the cavity boundary with time under the inflow condition, while the pH is around 9.0 under the no-inflow condition. The increase in pH with time within the fractures in both cases is also affected by the consumption of the H^+ ion which is induced by the occurrence of mineral dissolution (e.g., pressure solution). Moreover, for additional investigation of the spatial trend in the mineral dissolution, the field of solute concentrations in pore water were examined by focusing on the Al which is one of the major chemical species contained in target rock composition. In **Fig. 15,** the concentrations of Al (c_{Al} [mol/L]) in pore water at 0.001 years under the no-inflow condition and the inflow condition, are shown by log notation (i.e., $\log_{10}c_{\mathrm{Al}}$). As shown in the figure, in both cases, the Al concentrations within the fractures increase to roughly two orders of magnitude greater than the intact rock zone away from the cavity and it represents the influence by supply of the dissolved solute to concentrated fractured zone due to the mineral dissolution (e.g., pressure solution). In addition, the figure also shows that the concentration near the cavity under the inflow condition is greater than that under the no-inflow condition. The effect of the inflow-alkaline solution that made above mentioned difference in the concentration, are the spreading of the solute contained in the alkaline solution and the enhancement of the mineral dissolution rates within the fractures due to alkalization as confirmed in **Fig. 14**. Mainly due to the latter factor, the concentration within the fractures very close to the cavity under the inflow condition, rises at least three orders of magnitude greater than the intact rock zone away from the cavity. Such a result related to the enhancement of the mineral dissolution matches the spatial trend of promoted permeability drop under the inflow condition as indicated in **Figs. 12** and **13**. From **Figs. 11~15**, it is confirmed that the difference in the permeability evolution between the two cases (no-inflow condition and inflow condition) is significant only in the vicinity of the cavity in the early stage of the disposal period, and that it is brought about by the local enhancement of the pressure solution by an increase in the reaction rates depending on the pH value due to the spreading of the alkaline solution. The occurrence of these local trends is because of the great difference between the rate of pressure solution and the spreading rate of the alkaline solution. In the scheme of the pressure solution, expressed by Eqs. (25) and (32), the reaction stops at equilibrium when the stress acting on the asperity contacts within the fractures (contact stress) becomes equal to the critical stress. The time-dependent degradation of the contact stress to the critical stress is induced by an increase in the contact area linked to a decrease in the fracture aperture, as defined by Eq. (33). From **Fig. 11**, it can be expected that the rapid aperture reduction within the several fractures is caused by the pressure solution after the disposal of the waste package, and that after 0.1 years, the pressure solution would have already stopped within most fractures in both cases. Compared to the progress rate of the pressure solution until reaching equilibrium, the spreading rate of the alkaline solution from the cavity is very slow. Thus, the behavior of the pressure solution within the fractures only close to the cavity, to which the alkaline solution can reach immediately, is influenced by the inflow of the alkaline solution.

In order to further verify the above-mentioned insights, the changes in permeability and pH with time under the no-inflow condition and the inflow condition at two specific observation points (Points 1 and 2, see **Fig. 16**) within the fracture are depicted in **Figs. 17** and **18**. As shown in **Fig. 16**, Point 1 is installed in the vicinity of the cavity boundary, while Point 2 is set in a place a little away from the cavity boundary. As is apparent from **Figs. 17** and **18**, in the fracture close to the cavity (Point 1), the difference in the permeability reduction is significant in the early period (within the first 0.015 years) between the no-inflow condition and the inflow condition, while there is almost no difference in the fracture at a distance from the cavity (Point 2). This is because the alkaline solution has reached Point 1, but it has not reached Point 2 under the inflow condition. At Point 2, the pH evolution under the no-inflow condition is almost the same as that under the inflow condition and, in both cases, the permeability almost ends up at a converged value within the first 0.015 years. That is, at a distance from the cavity, the permeability reduction induced by the pressure solution has already been completed before the alkaline solution reaches. These results, observed at specific points, are consistent with the insights expected from **Figs. 11~15**.

Finally, in order to perform an integrated evaluation of the permeability reduction throughout the fracture zone, the spatially integrated permeability reduction is taken over the fracture domain at arbitrary time *t*, $\sum_{\Omega} \Delta k_f(t)$ [m^4], which is represented as follows:

$$\sum_{\Omega} \Delta k_f(t) = \int_{\Omega} \left[k_{f,i} - k_f(t) \right] dxdz \, . \tag{37}$$

where $k_{f,i}$ [m^2] is the permeability of the fracture domain at the initial condition in this analysis, and Ω is the entire fracture domain. The evolution in the spatially integrated permeability reductions over the fracture domain under no-inflow and inflow conditions is depicted in **Fig. 19**. As is apparent from the figure, in both cases, the amounts of integrated reductions rapidly increase in the early stages of the analysis period. Afterwards, they approach almost equal values. To focus on the difference in rates of reduction between the two cases in more detail, an extract of the early period in **Fig. 19** is shown in **Fig. 20**. This figure shows slight differences in the amounts/rates of reduction affected by the inflow of the alkaline solution, and the differences are a little clear to some extent within the first 0.02 years. Much of the difference may have been brought about by the enhancement of the pressure solution only close to the cavity due to the expansion of the alkaline solution.

4 Conclusion

In order to examine the impact of the inflow of the alkaline cement solution on the change in permeability over time within the fractured rocks at an actual field, a coupled THMC numerical model, *IPSACC*, that is able to address a series of permeability evolution, from fracture generation to subsequent geochemical creep, has been upgraded by incorporating the dependence of the geochemical reactions on the pH value. Then, the upgraded model was applied to predict the long-term alteration of the permeability in crystalline rock, which is located in geological disposal facilities of HLW. In the numerical predictions, the conditions of target subsurface were set by referring to the information obtained from an actual site in Mizunami area of Gifu, Japan, and they were assumed that also virtually consider the inflow of the alkaline cement solution from an artificial barrier. The predicted results showed that generation of many fractures during the cavity excavation increased the permeability by about two orders of magnitude, and that the permeability in the several shear-induced fractures was rapidly reduced by up to about two orders of magnitude within roughly 0.1 years afterwards with time due to the pressure solution at the contacting asperities of the fractures. The reduction in fracture permeability was locally accelerated only in the vicinity within about 0.2 m of the disposal cavity due to the significant alkalization of the groundwater induced by the inflow of the alkaline component. This is attributed to the fact that the alkaline component cannot arrive at the fractures, except near the disposal cavity, before the permeability reduction induced by the pressure solution quickly reaches the steady state. However, it should be noted that under assumed subsurface conditions in this study, the large compressive stress which significantly enhances the pressure solution can be occurred due to the several factors related to in-situ stress, such as a high-lateral pressure coefficient (K_0 = 1.6704) and a deep disposal depth (500 m). If the target environment has a smaller ground pressure, the time until that pressure solution reaches equilibrium is longer and the behavior of chemical-induced permeability evolution may be affected by the inflow of alkaline solution in a wider spatio-temporal range. In view of above, the performed numerical predictions suggest the possibility that, in the geological disposal of HLW under the high-ground pressure environments as assumed in this work, the influence of the inflow of the alkaline cement solution from an artificial barrier is spatiotemporally limited and is not dominant in the long-term performance of a natural barrier composed of crystalline rock for delaying the transport of radionuclides.

Numerical works based on the proposed model in this study, adopted several assumptions and simplifications for extremely complex coupled processes in actual rock masses, that are expected in geological disposal of HLW. For example, the proposed model only considers the geochemical impact induced by the mineral dissolution/precipitation for computing the time-dependent alteration of pore structure/permeability within rock masses. To grasp the permeability evolution more precisely, the mechanical impacts, such as the elastic deformation and fracture asperity degradation within rock masses, must be considered. In addition, because the fracturing process is computed only during the excavation stage of cavity, further occurrence of rock failure expected after disposing the waste package, such as fracture nucleation/growth induced by thermal stress, is not taken into account. Therefore, the attempting coupled simulations that is able to handle the fracturing process during cavity excavation and subsequent long-term disposal period, is needed for capturing the fractured zone within rock masses more realistically.

Acknowledgements

This work was supported by JSPS KAKENHI, subject nos.20K14826, and by the research grants funded by the Takahashi industrial and Economic Research Foundation, Research Institute for Environmental Geotechnics, FUKADA GEOLOGICAL INSTITUTE and MAEDA ENGINEERING FOUNDATION, Japan. Their support is gratefully acknowledged.

References

1. Japan Nuclear Cycle Development Institute, 2000: Second Progress Report on Research and Development for the Geological Disposal of HLW in Japan, Supporting Report 2 Repository Design and Engineering Technology, H12: Project to Establish the Scientific and Technical Basis for HLW Disposal in Japan. JNC TN1410 2000-003, IV-139-IV-160 (2000).
2. Aoyagi, K. and Ishii, E.: A Method for Estimating the Highest Potential Hydraulic Conductivity in the Excavation Damaged Zone in Mudstone. Rock Mech. Rock Eng. **52,** 385-401 (2019).
3. Zhang, C-H.: The stress-strain-permeability behaviour of clay rock during damage and recompaction. J. Rock Mech. Geotech. Eng. **8**, 16-26 (2016).
4. Tsang, C-F., Jing, L., Stephansson, O. and Kautsky, F.: The DECOVALEX III project: A summary of activities and-lessons learned. Int. J. Rock Mech. Min. Sci. **42**, 593-610 (2005).
5. Homand-Etienne, F. and Sebaibi, A.: Study of microcracking of the Lac du Bonnet granite. Eurock-ISRM Int. Symp. **2**, 1353-1362 (1996).
6. Souley, M., Homand, F., Peda, S. and Hoxha, D.: Damaged-induced permeability changes in granite: a case example at the URL in Canada. Int. J. Rock Mech. Min. Sci. **38**, 297-310 (2001).
7. Kelsall, PC., Case, JB. and Chabanne, CR.: Evaluation of excavation induced changes in permeability. Int. J. Rock Mech. Min. Sci. **21**, 121-135 (1984).
8. Bauer, C., Homand, F. and Henry, JP.: In situ low permeability pulse test measurements. Int. J. Rock Mech. Min.

Sci. **32**, 357-63 (1995).

9. Tsang, CF., ed.: *Coupled Processes Associated with Nuclear Waste Repositories*. Amsterdam: Elsevier, 2012.

10. Tsang, Y.: Effects of coupled processes on a proposed high-level radioactive waste repository at Yucca Mountain, Nevada. *Geol Soc Am Memorie*. **209**, 363-393 (2012).

11. Polak, A., Elsworth, D., Yasuhara, H., Grader, A. and Halleck, P.: Permeability reduction of a natural fracture under net dissolution by hydrothermal fluids. Geophys. Res. Lett. **30** (20), 2020, doi:10.1029/2003 GL017575 (2003).

12. Polak, A., Elsworth, D., Yasuhara, H., Grader, AS. and Halleck, PM.: Spontaneous switching of permeability changes in a limestone fracture with net dissolution. Water Resour. Res. **40**, W03502, doi:10.1029/ 2003WR002717 (2004).

13. Yasuhara, H., Elsworth, D. and Polak, A.: Evolution of permeability in a natural fracture: the significant role of pressure solution. J. Geophys. Res. **109**, B03204, doi:10.1029/2003JB002663 (2004).

14. Yasuhara, H., Kinoshita, N., Ohfuji, H., Lee, DS., Nakashima, S. and Kishida, K.: Temporal alteration of fracture permeability in granite under hydrothermal conditions and its interpretation by coupled chemo-mechanical model. Appl. Geochem. **26**, 2074-2088 (2011).

15. Yasuhara, H. and Elsworth, D.: A numerical model simulating reactive transport and evolution of fracture permeability. Int. J. Numer. Anal. Methods Geomech. **30**, 1039-1062 (2006).

16. Yasuhara, H., Elsworth, D., Polak, A., Liu, J., Grader, A. and Halleck, P.: Spontaneous permeability switching in

fractures in carbonate: lumped parameter representation of mechanically and chemically mediated dissolution. Transp Porous Media. **65**: 385–409 (2006).

17. Robert, AC., Ehsan, G., Julia, NP. and Nico, P.: Experimental investigation of fracture aperture and permeability change within Enhanced Geothermal Systems. Geothermics. **62**, 12–21(2016).
18. Beeler, MN. and Hickman, SH.: Stress-induced, time-dependent fracture closure at hydrothermal conditions. J. Geophys. Res. **109**(B3): B02211 doi:10.1029/2002JB001782 (2004).
19. Kinoshita, N. and Yasuhara, H.: Evolution of Fracture Permeability in Granite under High Temperature and High Confining Pressure Condition, Journal of MMIJ. **128**, 72-78 (2012).
20. Yasuhara, H., Hashimoto, K. and Kinoshita, N.: Evaluation of Dissolution Equation in Granite Examination by Flow-Through Dissolution Experiment under Temperature and pH conditions Controlled, Journal of MMIJ, 128, 79-85 (2012).
21. Palandri, JL. and Kharaka, YK.: A compilation of rate parameters of mineral-water interaction kinetics for application to geochemical modelling. US Geological Survey open file report 2004–108, USA (2004).
22. Knauss, K.G.and Wolery, T.J.: Dependence of albite kinetics on pH and time at 25℃ and 70 °C. Geochem. Cosmochim. Act, 50, 2481-2497 (1986).
23. Fenter, P., Park, C., Cheng, L., Zhang, Z., Krekeler, M.P.S. and Sturchio, N.C.: Orthoclase dissolution kinetics probed by in situ X-ray reflectivity: Effects of temperature, pH, and crystal orientation. Geochim. Cosmochim. Act, 67, 197-211 (2003).

24. Knauss, K.G.Knauss and Wolery, T.J.: Experimental study of anorthite dissolution and the relative mechanism of feldspar hydrosis. Geochem. Cosmochim. Act, 59, 5039-5053 (1995).

25. Rutqvist, J., Wu, Y-S., Tsang, C-F. and Bodvasson, G.: A modeling approach for analysis of coupled multiphase fluid flow, heat transfer, and deformation in fractured porous rock. Int. J. Rock Mech. Min. Sci. **39**, 429-442 (2002).

26. Suzuki, H., Nakama, S., Fujita, T., Imai, H. and Sazarshi, M.: A long-term THMC assessment on the geochemical behavior of the bentonite buffer. J. Nucl Fuel Cycle. Environ, **19**, 39-50 (2012).

27. Nasir, O., Fall, M. and Evgin, E.: A simulator for modeling of porosity and permeability changes in near field sedimentary host rocks for nuclear waste under climate changes influences. Tunneling and Underground Space Technology. **42**, 122-135 (2014).

28. Fall, M., Nasir, O. and Nguyen, T. S.: A coupled hydro-mechanical model for simulation of gas migration in host sedimentary rocks for waste repositories. Eng. Geol. **176**, 24-44 (2014).

29. Zhang, R., Yin, X., Winterfeld, P. H. and Wu, Y.-S.: A fully coupled thermal-hydrological-chemical model for CO_2 geological sequestration. J. Nat. Gas Sci. Eng. **28**, 280-304 (2016).

30. Ogata, S., Yasuhara, H., Kinoshita, N., Cheon, DS. and Kishida, K.: Modeling of coupled thermal-hydraulic-mechanical-chemical process for predicting the evolution in permeability and reactive transport behavior within single rock fractures., Int. J. Rock Mech. Min. Sci. **107**, 271-281 (2018).

31. Wei, CH., Zhu, WC. Chen, S. and Ranjith, PG.: A coupled thermal-hydrological-mechanical damage model and its numerical simulations of damage evolution in APSE. Materials. **9**, 841, doi: 10.3390/ma9110841 (2016).

32. Li, LC., Tang, CA., Wang, SY. and Yu, J.: A coupled thermo-hydrologic-mechanical damage model and associated application in a stability analysis on a rock pillar. Tunneling and Underground Space Technology. **34**, 38-53 (2013).

33. Wei, CH., Zhu, WC., Yu, QL., Xu, T. and Jeon, S.: Numerical simulation of excavation damaged zone under coupled thermal-mechanical conditions with varying mechanical parameters. Int. J. Rock Mech. Min. Sci. **75**, 169-181 (2015).

34. Poulet, T., Karrech, A., Lieb, RK., Fisher, L. and Schaubs, P.: Thermal-hydraulic-mechanical-chemical coupling with damage mechanics using ESCRIPTRT and ABAQUAS. Tectonophysics. 124-132 (2013).

35. Marschall, P., Giger, S., Vassiere, DLR., Shao, H., Leung, H., Nussbaum, C., Trick, T., Lanyon, B., Senger, R., Lisjak, A. and Alcolea, A.: Hydro-mechanical evolution of the EDZ as transport path for radionuclides and gas: insights from the Mont Terri rock laboratory (Switzerland). Swiss J. Geosci. **110**, 173-194 (2017).

36. Yasuhara, H., Kinoshita, N., Ogata, S., Cheon, DS. and Kishida, Kiyoshi.: Coupled thermo-hydro-mechanical-chemical modeling by incorporating pressure solution for estimating the evolution of rock permeability, Int. J. Rock Mech. Min. Sci. **86**, 104-114 (2016).

37. Taron, J., Elsworth, D. and Min., KB.: Numerical simulation of thermal-hydrologic-mechanical-chemical processes in deformable fractured porous media. Int. J. Rock Mech. Min. Sci. **46**, 842-854 (2009).

38. Renchao, L., Thomas, N., Hua S., Olaf, K. and Haibing S.: Modeling of Dissolution-Induced Permeability Evolution of a Granite Fracture Under Crustal Conditions. J. Geophys. Res. **123**, 5609-5627 (2018).

39. Weitao, L., Jiyuan, Z., Ruiai, N., Yifan, Z, Baichao, X. and Xi, S.: A Full Coupled Thermal-Hydraulic-Chemical

Model for Heterogeneity Rock Damage and Its Application in Predicting Water Inrush. Appl. Sci. 9, 2195; doi:10.3390/app9112195 (2019).

40. Ogata, S., Yasuhara, H., Kinoshita, N. and Kishida, K. : Coupled thermal–hydraulic–mechanical–chemical modeling for permeability evolution of rocks through fracture generation and subsequent sealing, Computational Geosciences, **24**, 1845-1864, https://doi.org/10.1007/s10596-020-09948-3 (2020).
41. Ogata, S., Yasuhara, H. and Kishida, K.: Coupled THMC analysis for porous rock by considering damage theory, *Journal of JSCE* (section C), **75**, 131-145 (2019).
42. Tang, CA.: Numerical simulation on progressive failure leading to collapse and associated seismicity. Int. J. Rock Mech. Min. Sci. **34**, 249-262 (1997).
43. Tang, CA., Liu, H., Lee, KKP., Tsui, Y. and Tham, LG.: Numerical studies of the influence of microstructure on rock failure in uniaxial compression- Part I : effect of heterogeneity. Int. J. Rock Mech. Min. Sci. **37**, 555-569 (2000).
44. Zhu, WC. and Tang, CA.: Micromechanical model for simulating the fracture process of rock. Rock Mech. Rock Eng. **37**, 25-56 (2004).
45. Li, G. and Tang, CA.: A statistical meso-damage mechanical method for modeling trans-scale progressive failure process of rock. Int. J. Rock Mech. Min. Sci. **74**, 133-150 (2015).
46. Liu, HY., Roquete, M., Kou, SQ. and Lindqvist, PA.: Characterization of rock heterogeneity and numerical verification. Eng. Geol. **72**, 89-119 (2004).
47. Wang, SY., Sloan, SW., Scheng, DC., Yang, SQ. and Tang, CA.: Numerical study of failure behavior of pre-cracked

rock specimens under conventional triaxial compression. Int. J. Solids Struct. **51**, 1132-1148 (2014).

48. Wang, J., Elsworth, D., Wu, Yu., Liu, Jishan., Zhu, WC. and Liu, Y.: The Influence of Fracturing Fluids on Fracturing Processes: A Comparison Between Water, Oil and SC-CO_2.Rock. Mech. Rock. Eng. **51**, 299-313 (2018).
49. Weibull, W.: A statistical distribution function of wade applicability. J. Appl. Mech. **18**, 293-297 (1951).
50. Zhu, WC., Weu, C., Li, S., Wei, J. and Zhang, M.: Numerical modeling on destress blasting in coal seam for enhancing gas drainage, Int. J. Rock Mech. Min. Sci. **59**, 179-190 (2013).
51. Bear, J.: Dynamics of Fluids in Porous Media, Dover Publications. 161-176 (1972)
52. Revil, A.: Pervasive pressure-solution transfer: a poro-visco-plastic model. Geophys. Res. Lett. **26**, 255-258 (1999).
53. Lasaga, AC.: Chemical kinetics of water-rock interactions. J. Geophys. Res. **89**, 4009-4025 (1984).
54. Cocks, A. and Ashby, M.: Intergranular fracture during power-law creep under multiaxial stresses. Metal Science. **14**, 395-402 (1980).
55. Gohke, M., Horita M., Wakabayashi N. and Nakatani A.: Excavation disturbance analysis based on Crack Tensor Model and Virtual Fracture Model for predicting the rock mass behavior during excavation of shafts and research galleries at the Mizunami Underground Research Laboratory. JNC TJ7400. 2005-058 (2005).
56. Detounay, E. and Cheng, A.H.-D.: Fundament poroelasticity. in Comprehensive Rock Engineering: Principals, Practice and Projects, 2 edited by Hudson, J.A., Pergamon Press, Oxford. 113-171 (1993).
57. Halt, D.J. and Wang., H.F.: Laboratory measurements of a complete set of poroelastic moduli for Brea sandstone

and Indiana limestone, J. Geophy. Res., **100**, 17741-17751 (1995).

58. Kosaka, H., Saegusa, H., Onoue, H. and Takeuchi, R.: Study on Hydrogeology on the Mizunami Underground Research Laboratory Project Hydrogeological Modeling and Groundwater Flow Simulation for Planning of Long-term Pumping Test. JAEA-Research, 2010-037 (2011).

59. Sato, T., Taniguchi, W., Fujita, T. and Hasegawa, H.: Data Collection by Literature Survey on Rock Physics Properties in Japan (Ⅱ). JNC TN7400 99-011 (1999).

60. COMSOL2014：COMSOL MULTIPHYSICS. Version 5.0, Available from www.comsol.com (2004).

61. Parkhurst, DL. and Appelo, CAJ.: Description of Input and Examples for PHREEQC Version3-A Computer Program for Speciation, Batch-Reaction, One-Dimensional Transport, and Inverse Geochemical Calculations, Online version availableromhttp://wwwbrr.cr.usgs.gov/projects/GWC_coupled/phreeqc/phreeqc3-html/phreeq-c3.htm.

62. Azad, Vj., Li, C., Verba, C., ldeker, JH. and lsgor, OB.: A COMSOL-GEMS interface for modeling coupled reactive-transport geochemical processes. Comput. Geosci-UK. **92**, 79-89 (2016).

63. Gohke, M., Horita M., Wakabayashi N. and Nakatani A.: Excavation disturbance analysis based on Crack Tensor Model and Virtual Fracture Model for predicting the rock mass behavior during excavation of shafts and research galleries at the Mizunami Underground Research Laboratory. JNC TJ7400. 2005-058 (2004).

64. Li L., Perters CA. and Celia MA.: Upscaling geochemical reaction rates using pore-scale network modeling. Advances in water resources. **29**, 1351-1370 (2006).

65. JNC (Japan Nuclear Cycle Development Institute), 2005: Development and management of the technical knowledge base for the geological disposal of HLW, Summary of the H17 project reports. Vol. 1. Scientific research of deep underground. JNC TN1400 2005-014 (2005) .

66. Suzuki, H., Ito, A., Yoshida, Y., Suyama, T., Kawakami, S., Sasamoto, H. and Yui, M.: Experimental Studies on the Coupled THMC Processes by COUPLE Equipment - Part I -. JNC-TN8400 2003-033 (2004) .

67. Atkinson, A., Hearne J.A. and Knights, C. F.: Aqueous chemistry and thermodynamic modeling of CaO-SiO_2-H_2O gel, AERER12543 (1987).

68. Hayashida, K., Kato, T., Kubota, M., Murakami, H., Amano, Y. and Iwatsuki, T.: Evaluation of hydrogeochemical proceeses provoked by tunnel excavation and closure based on simulated experiment in a mock-up test drift. Chikyukagaku (Gecgemistly). **59**, 55-71 (2018).

Tables and Figures

Tables

Table 1 Parameters used in simulation.

Note: The bulk modulus of fluid K_f was set to the general value of water and critical stress σ_c was set to be equivalent to the uniaxial compressive strength of the target rock.

Table 2 Parameters of kinetic dissolution rate constant [21, 64].

Note: The data on the anorthite and other minerals were obtained from Li et al. (2006) [64] and Palandri and Kharaka (2004) [21], respectively.

Table 3 Chemical composition of alkaline cement solution from cavity boundary (Inlet boundary) [66, 67].

Table 4 Initial chemical composition of groundwater utilized in simulation [68].

Figures

Fig. 1 THMC coupled interactions addressed in the presented model. The components expressed in blue letters were not addressed in our previous model [40].

Fig. 2 Constitutive law of damage theory under uniaxial tensile stress and uniaxial compressive stress (illustrated in Li et al., 2013 [32]).

Fig. 3 Geometrical model that includes representative element in rock fracture area [13].

Fig. 4 Numerical domain for long-term simulations.

Fig. 5 Description of excavation analysis.

Fig. 6 Evolution of damaged zone during cavity excavation.

Fig. 7 Temperature depending on time T_b (t) set as boundary condition at periphery of cavity [1].

Fig. 8 Boundary conditions of long-term coupled THMC simulations.

Fig. 9 Change in permeability distribution around cavity with time in range of 0 – 4.0 years under (a) no-inflow condition and (b) inflow condition.

Fig. 10 Permeability distributions around cavity at initial state and after 1.0 years in case considering inflow condition, which does not consider occurrence of pressure solution.

Fig. 11 Change in normalized permeability distribution around cavity with time in range of 10^{-3}–1.0 years under (a) no-inflow condition and (b) inflow condition.

Fig. 12 Normalized permeability distributions focused near invert at 0.001 years after disposal of waste package under (a) no-inflow condition and (b) inflow condition.

Fig. 13 The change in ratio of permeability distribution within fractures under inflow condition and that under no-inflow condition with time in range of 10^{-3}-0.1 years.

Fig. 14 Change in pH distribution within fractures with time in range of 0 – 0.1 years under (a) no-inflow condition and (b) inflow condition.

Fig. 15 Distribution of Al concentrations at 0.001 years under (a) no-inflow condition and (b) inflow condition.

Fig. 16 Setting the observation points. Points 1 and 2 are set in the computed fracture zone where the permeability reduction occurs over time. Point 1 is set in the vicinity of the cavity and Point 2 is set in a place a little away from the cavity.

Fig. 17 Changes in permeability and pH within first 0.1 years under no-inflow condition and inflow condition at observation point (Point 1) in fracture zone depicted in **Fig. 16.**

Fig. 18 Changes in permeability and pH within first 0.1 years under no-inflow condition and inflow condition at observation point (Point 2) in fracture zone depicted in **Fig. 16.**

Fig. 19 Changes in space-integrated permeability reduction within 1.0 years under no-inflow condition and inflow condition.

Fig. 20 Changes in space-integrated permeability reduction within first 0.1 years under no-inflow condition and inflow condition.

Table 1 Parameters used in simulation.

Parameter	Value
Homogeneity index of material properties [-] m	2.0 [44, 46]
Characteristic value of elastic modulus [GPa] $E_0{}^s$	50.3 [55]
Characteristic value of uniaxial tensile strength [MPa] $f_{t0}{}^s$	5.36 [55]
Characteristic value of uniaxial compressive strength [MPa] $f_{c0}{}^s$	159.6 [55]
Internal friction angle [°] θ	52.6 [55]
Poisson’s ratio [-] v	0.27 [55]
Bulk modulus of solid [GPa] K_s	40 [56, 57]
Bulk modulus of fluid [GPa] K_f	2.0
Permeability of the undamaged rock [m^2] k_0	1.82×10^{-16} [58]
Initial porosity [%] φ_i	1.12 [55]
Initial thermal conductivity of the solid [$w\ m^{-1}\ K^{-1}$] λ_{m0}	3.0 [59]
Heat capacity of the solid [$kJ\ kg^{-1}\ K^{-1}$] $C_{p,m}$	0.8 [59]
Thermal expansion coefficient of solid [K^{-1}] α_T	1.15×10^{-5} [59]
Coefficient that represents the damage-permeability effect [-] α_k	5.0 [48]
Coefficient that represents the damage-solid thermal conductivity [-] α_λ	5.0 [31]
Roughness factor [-] f_r	7.12 [14]
Critical stress [MPa] σ_c	150 [55]
Pre-exponential factor of diffusion of solute [$m^2\ s^{-1}$] D_b^0	5.2×10^{-8} [52]
Activation energy of diffusion of solute [$kJ\ mol^{-1}$] E_D	13.5 [52]
Constant [-] a	0.04 [14]

Note: The bulk modulus of fluid K_f was set to the general value of water and critical stress σ_c was set to be equivalent to the uniaxial compressive strength of the target rock.

Table 2 Parameters of kinetic dissolution rate constant [21, 64].

Parameter	Quartz	K-feldspar	Anorthite	Albite	Biotite	Amorphous silica
$\log k_1^{298.15K}$		-10.66	-3.32	-10.16	-9.84	
$\log k_2^{298.15K}$	-13.99	-12.56	-11.6	-12.56	-12.55	-12.3
$\log k_3^{298.15K}$		-21.2	-13.5	-15.6	-	
E_1 [kJ/mol]		51.7	18.4	65	22.0	
E_2 [kJ/mol]	87.6	38.0	18.4	69.8	22.0	76.0
E_3 [kJ/mol]		94.1	18.4	71.0	-	
n_1		0.50	1.5	0.457	0.525	
n_3		-0.823	-0.33	-0.572	-	

Note: The data on the anorthite and other minerals were obtained from Li et al. (2006) [64] and Palandri and Kharaka (2004) [21], respectively.

Table 3 Chemical composition of alkaline cement solution from cavity boundary (Inlet boundary) [66, 67].

Inlet water composition	Value
Al [mol L^{-1}]	1.30×10^{-3}
Ca [mol L^{-1}]	5.35×10^{-3}
K [mol L^{-1}]	5.81×10^{-2}
Na [mol L^{-1}]	3.76×10^{-2}
Si [mol L^{-1}]	1.19×10^{-4}
Mg [mol L^{-1}]	6.08×10^{-9}
S [mol L^{-1}]	1.19×10^{-6}
Cl [mol L^{-1}]	2.30×10^{-3}
C [mol L^{-1}]	1.32×10^{-3}
pH	12.90

Table 4 Initial chemical composition of groundwater utilized in simulation [68].

Initial pore water composition	Value
Al [mol L^{-1}]	1.9×10^{-5}
Mn [mol L^{-1}]	3.6×10^{-7}
K [mol L^{-1}]	2.0×10^{-5}
Na [mol L^{-1}]	7.8×10^{-3}
Si [mol L^{-1}]	3.0×10^{-4}
Ca [mol L^{-1}]	2.1×10^{-3}
Mg [mol L^{-1}]	6.0×10^{-6}
Fe [mol L^{-1}]	4.0×10^{-5}
F [mol L^{-1}]	3.0×10^{-4}
Cl [mol L^{-1}]	1.2×10^{-2}
S [mol L^{-1}]	5.0×10^{-6}
N [mol L^{-1}]	2.2×10^{-5}
pH	8.59

.

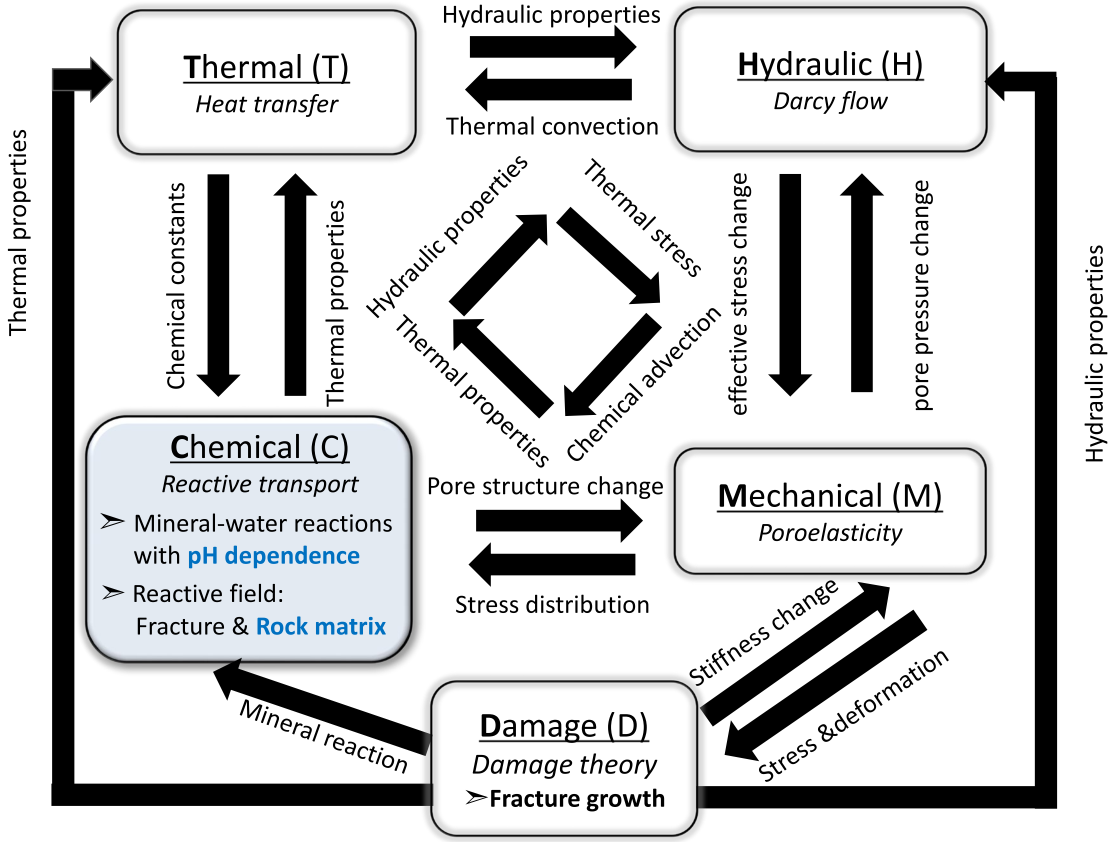

Fig. 1 THMC coupled interactions addressed in the presented model. The components expressed in blue letters were not addressed in our previous model [40].

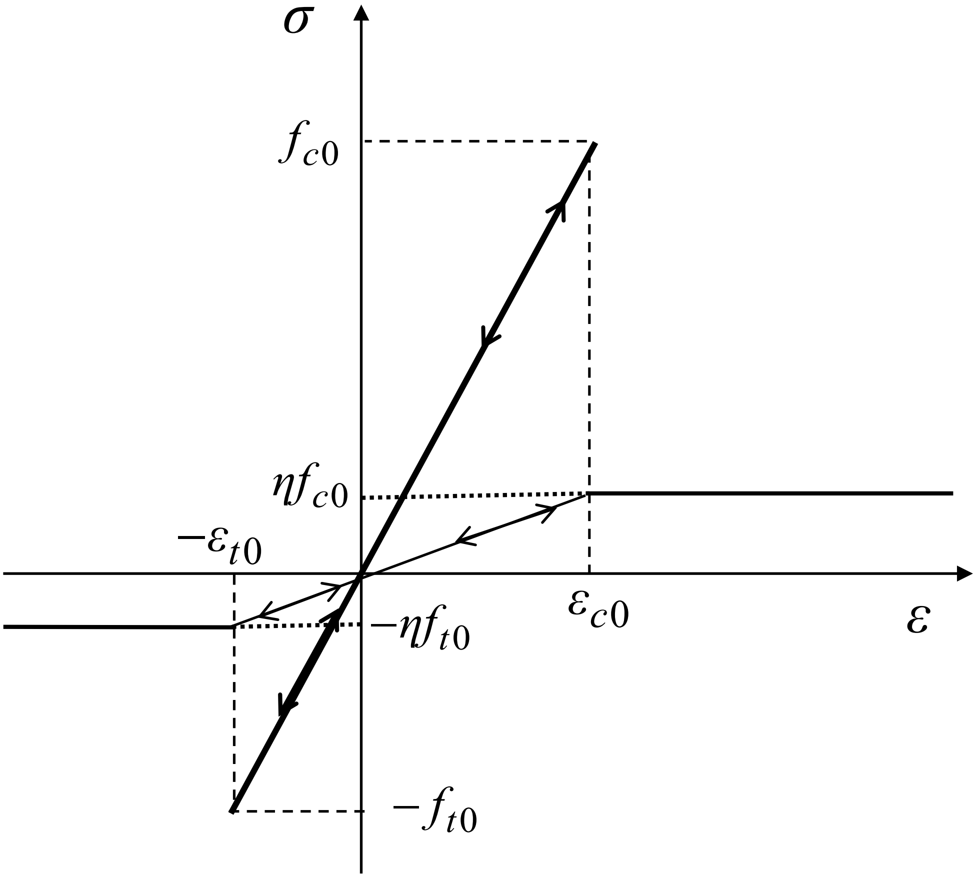

Fig. 2 Constitutive law of damage theory under uniaxial tensile stress and uniaxial compressive stress (illustrated in Li et al., 2013 [32]).

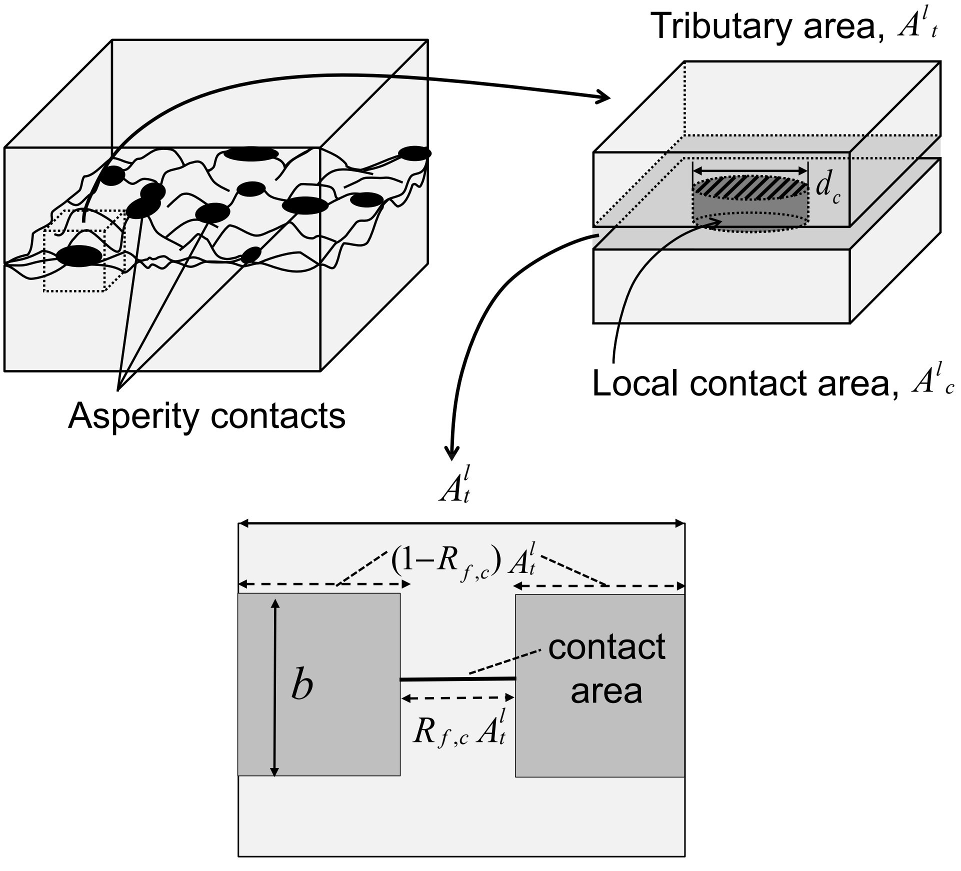

Fig. 3 Geometrical model that includes representative element in rock fracture area [13].

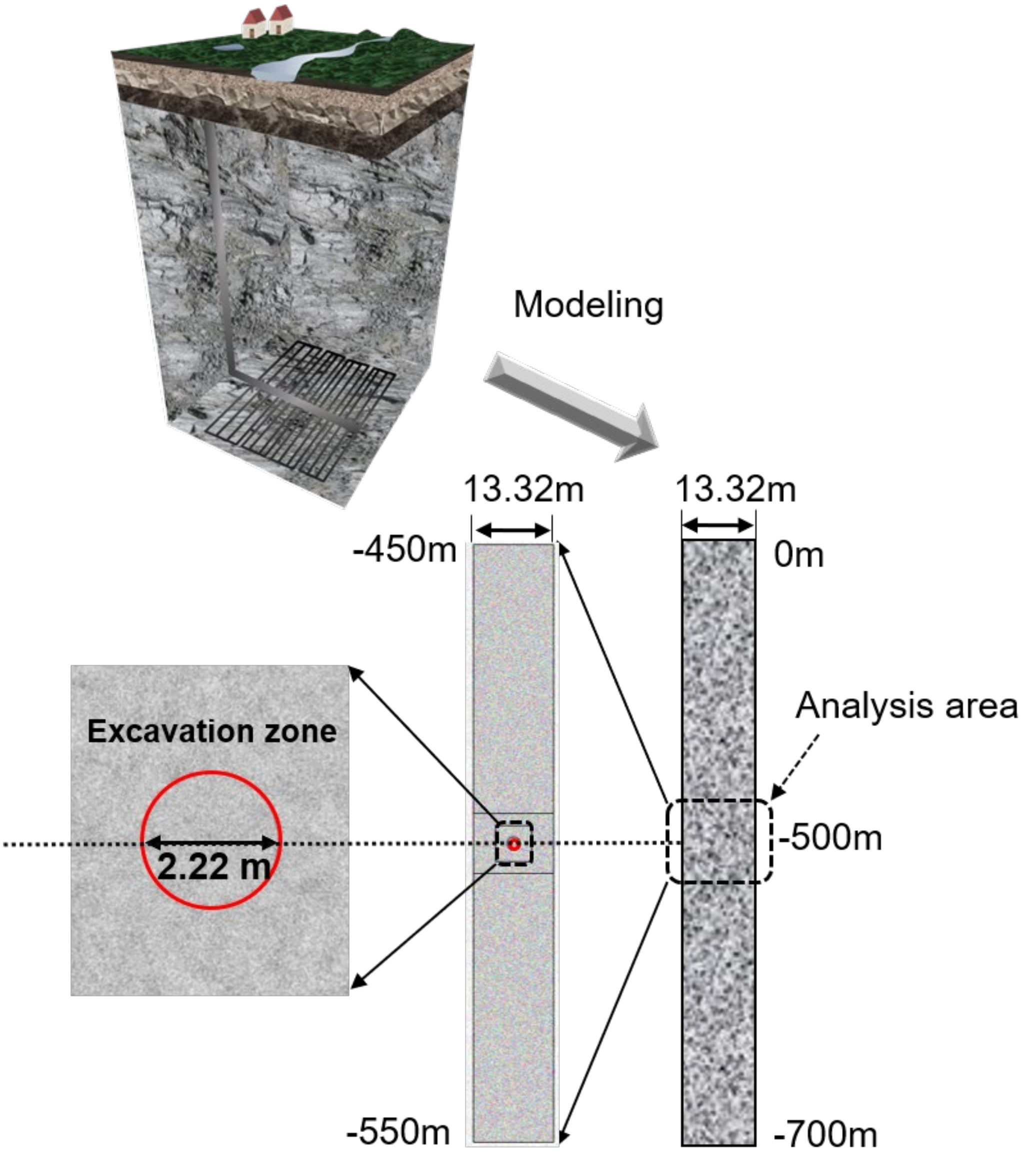

Fig. 4 Numerical domain for long-term simulations.

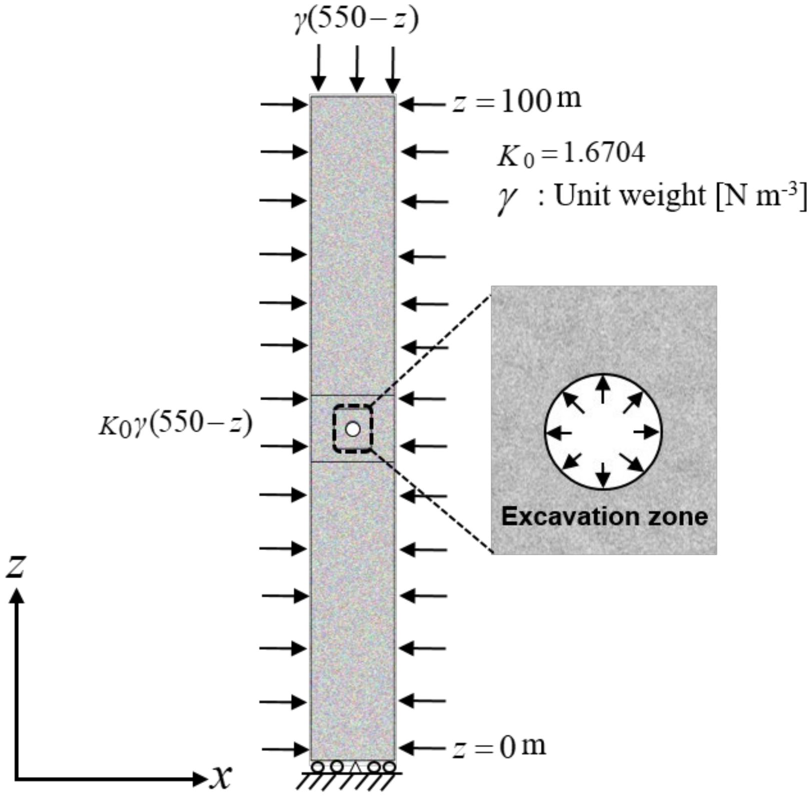

Fig. 5 Description of excavation analysis.

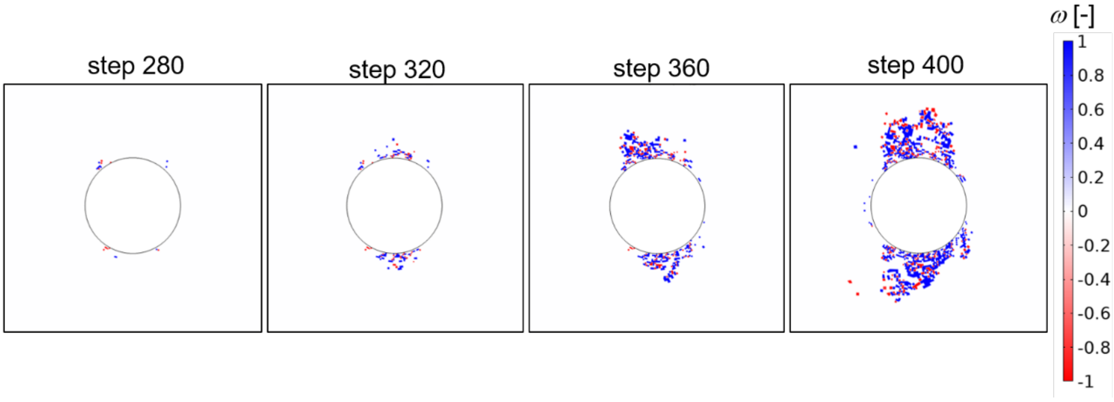

Fig. 6 Evolution of damaged zone during cavity excavation.

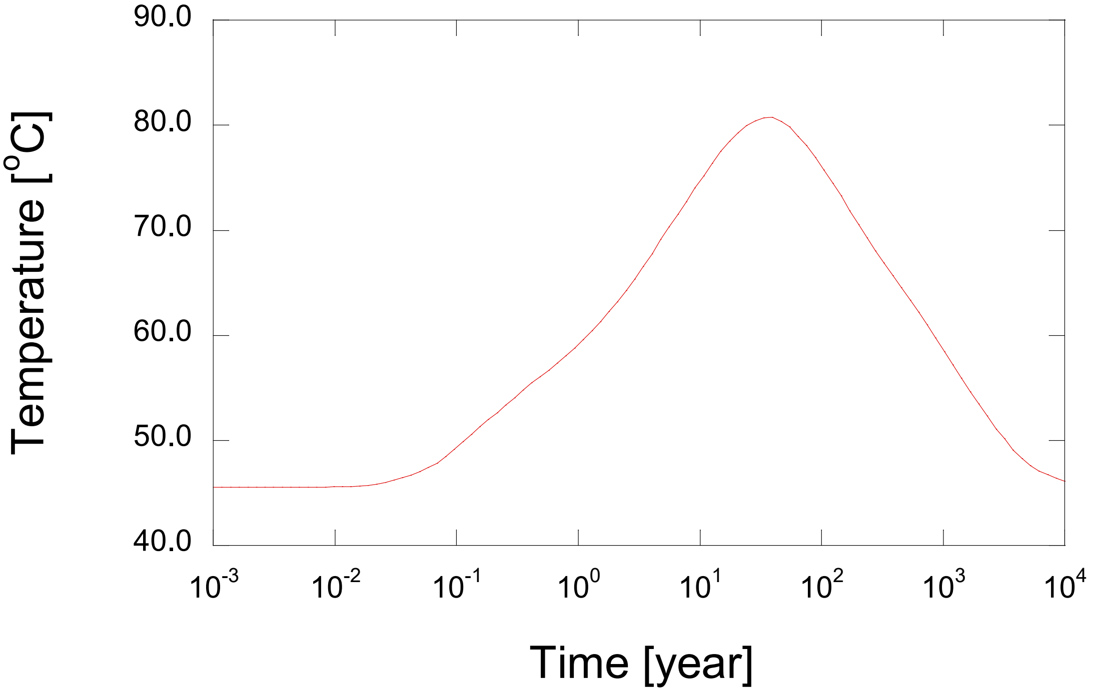

Fig. 7 Temperature depending on time T_b (t) set as boundary condition at periphery of cavity [1].

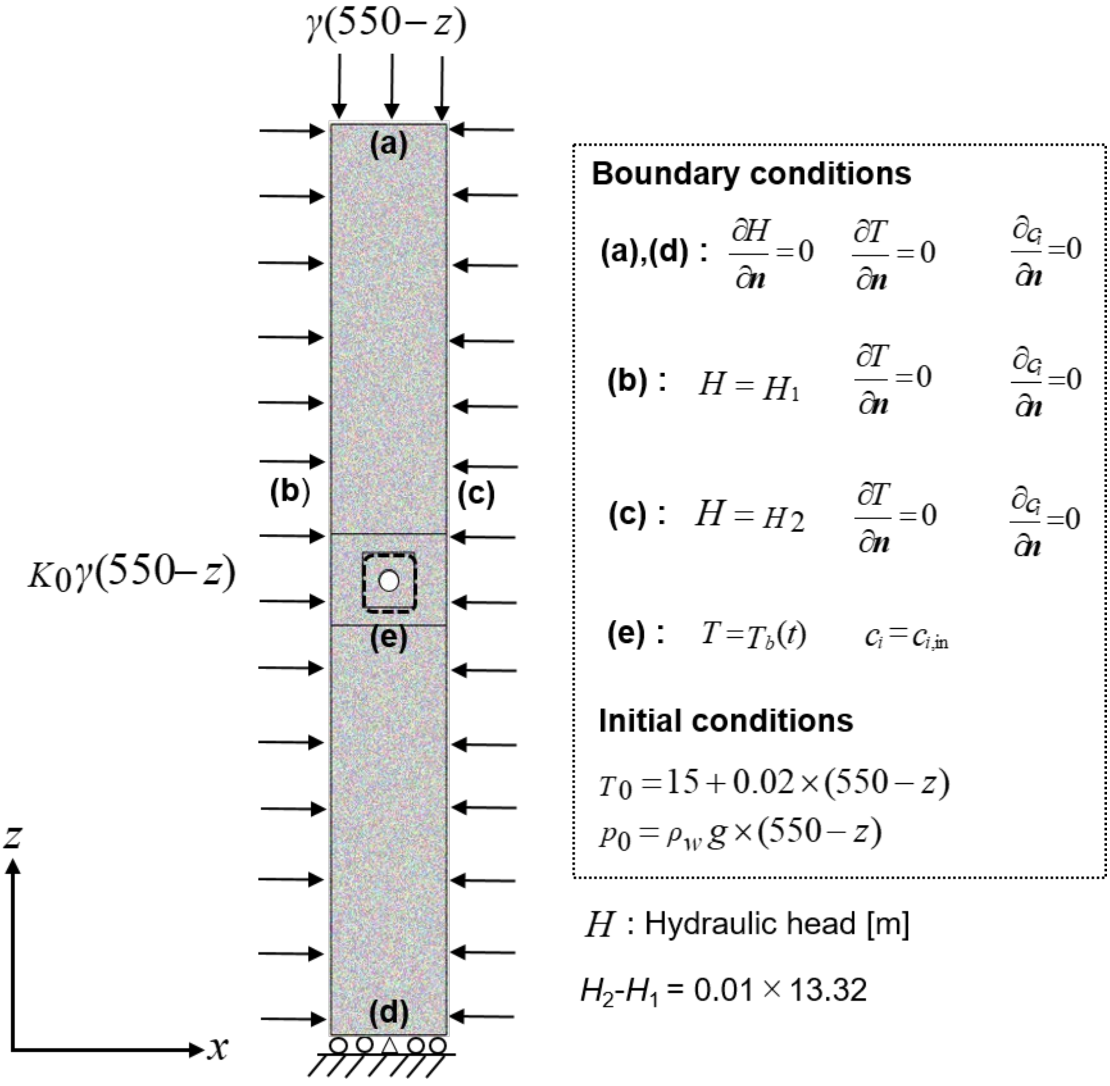

Fig. 8 Boundary conditions of long-term coupled THMC simulations.

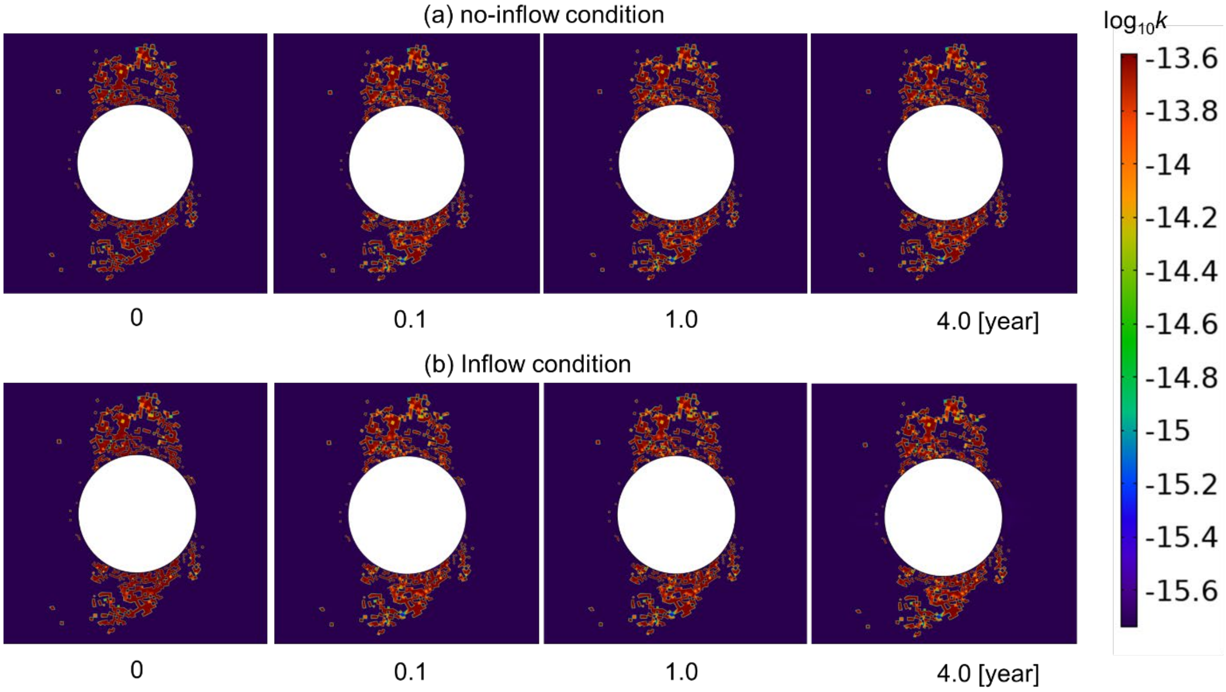

Fig. 9 Change in permeability distribution around cavity with time in range of 0 – 4.0 years under (a) no-inflow condition and (b) inflow condition.

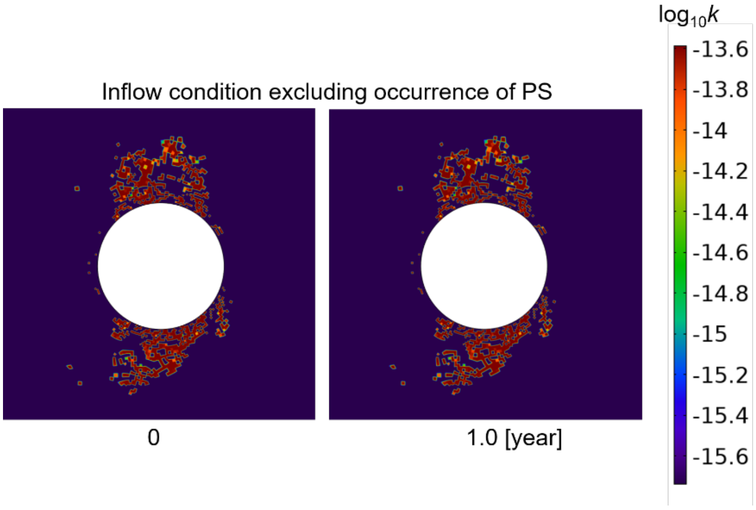

Fig. 10 Permeability distributions around cavity at initial state and after 1.0 years in case considering inflow condition, which does not consider occurrence of pressure solution.

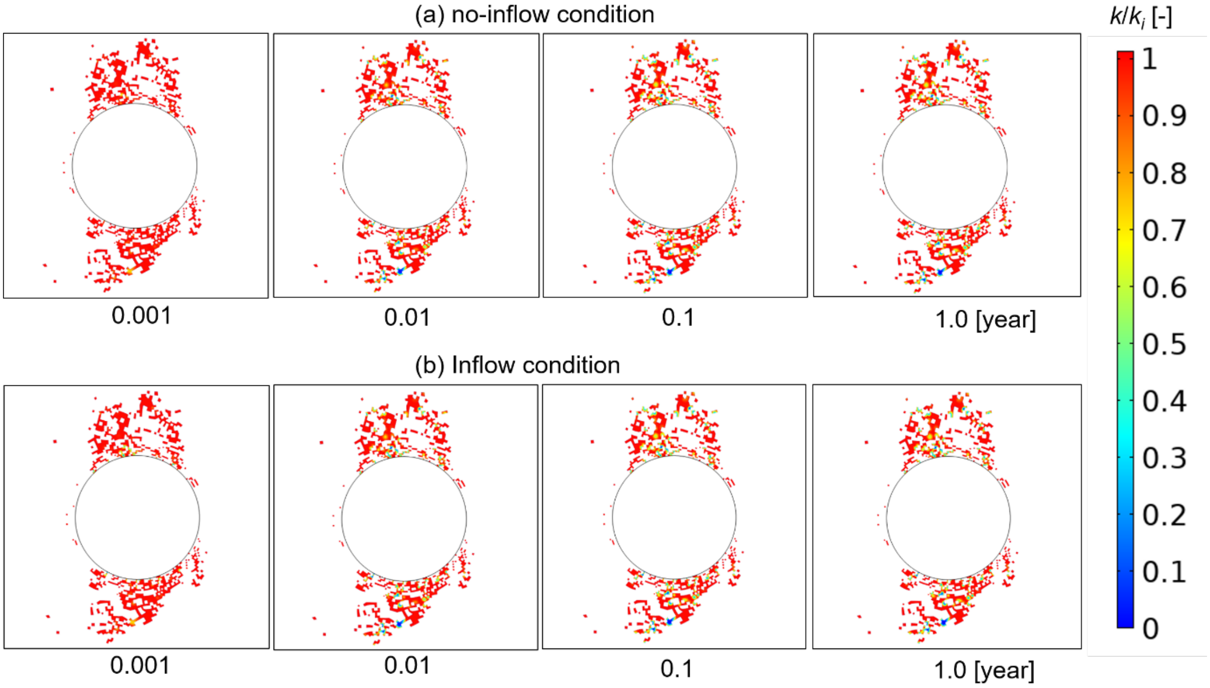

Fig. 11 Change in normalized permeability distribution around cavity with time in range of 10^{-3}–1.0 years under (a) no-inflow condition and (b) inflow condition.

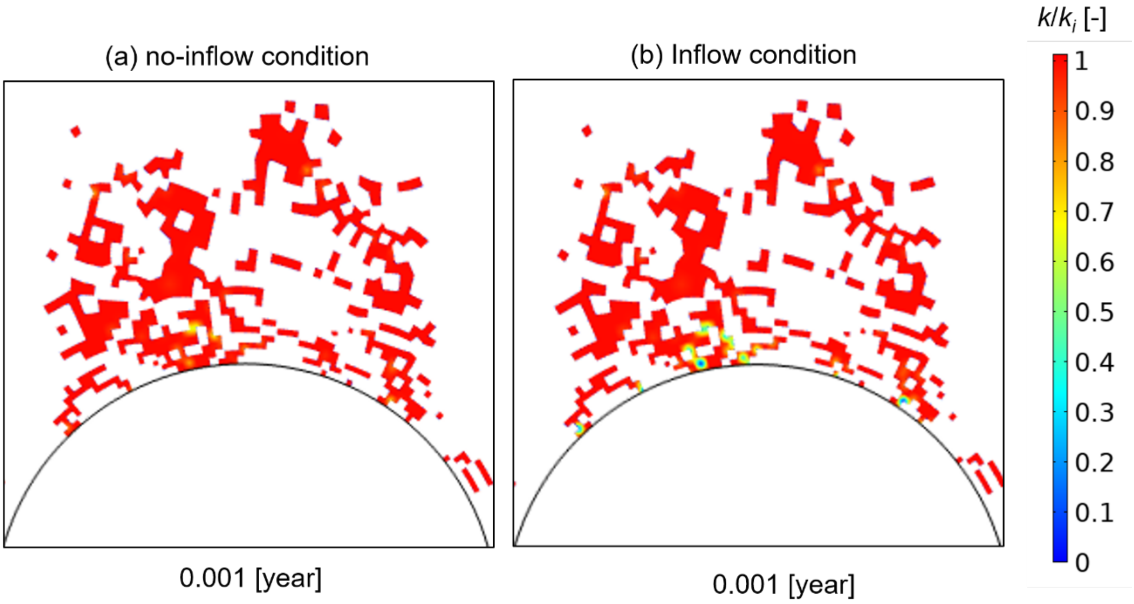

Fig. 12 Normalized permeability distributions focused near invert at 0.001 years after disposal of waste package under (a) no-inflow condition and (b) inflow condition.

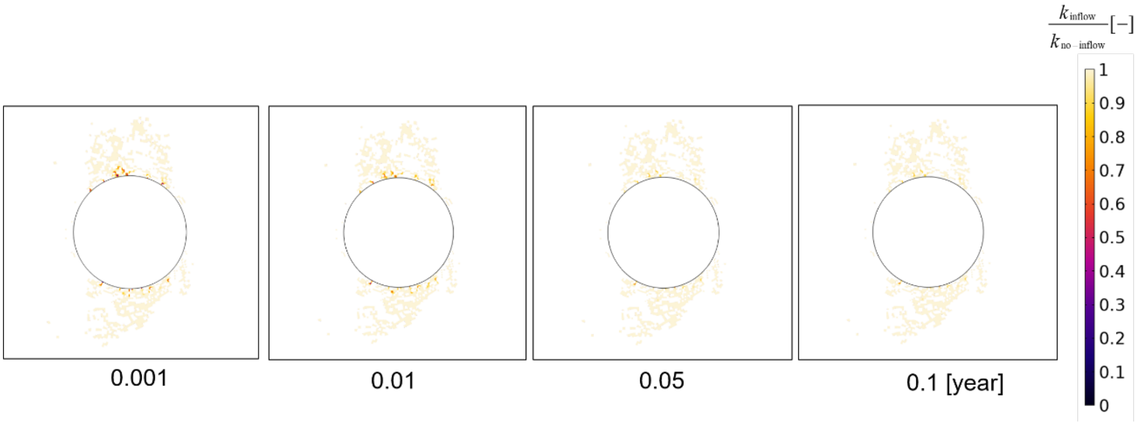

Fig. 13 The change in ratio of permeability distribution within fractures under inflow condition and that under no-inflow condition with time in range of 10^{-3}–0.1 years.

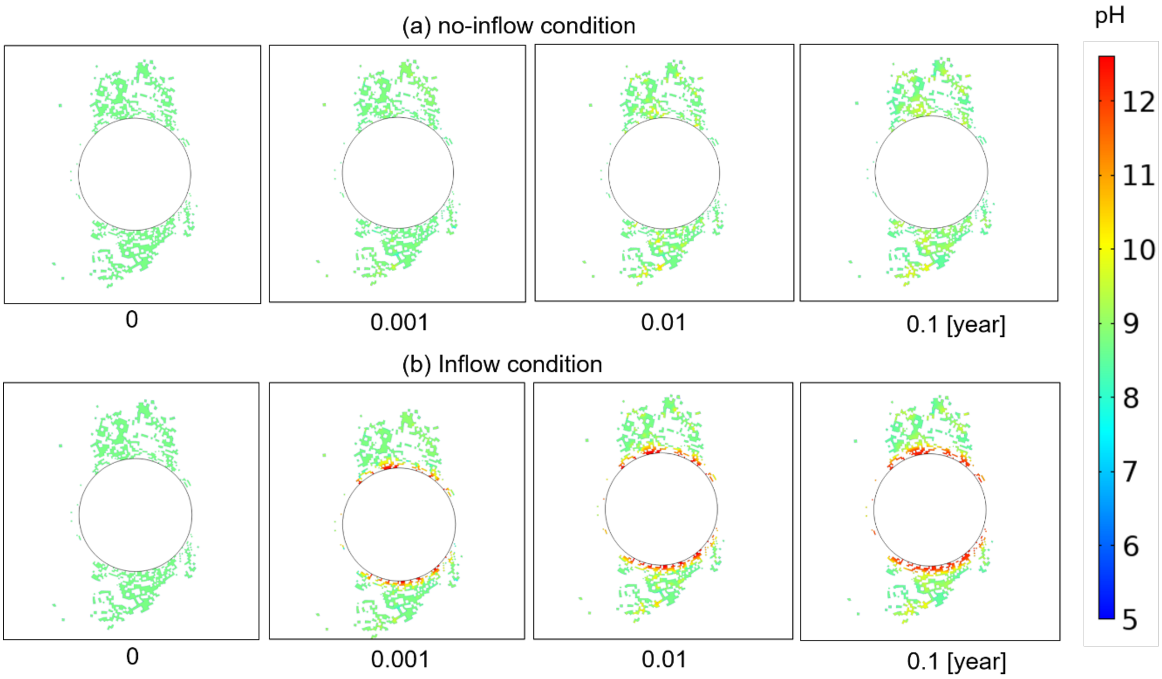

Fig. 14 Change in pH distribution within fractures with time in range of 0 – 0.1 years under (a) no-inflow condition and (b) inflow condition.

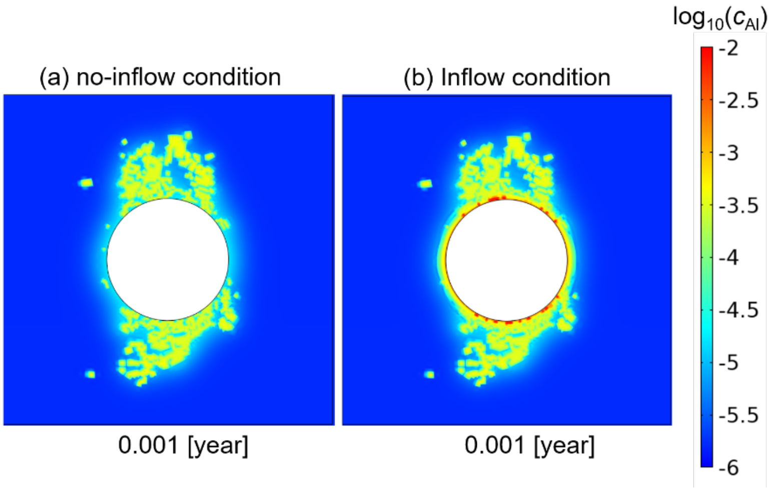

Fig. 15 Distribution of Al concentrations at 0.001 years under (a) no-inflow condition and (b) inflow condition.

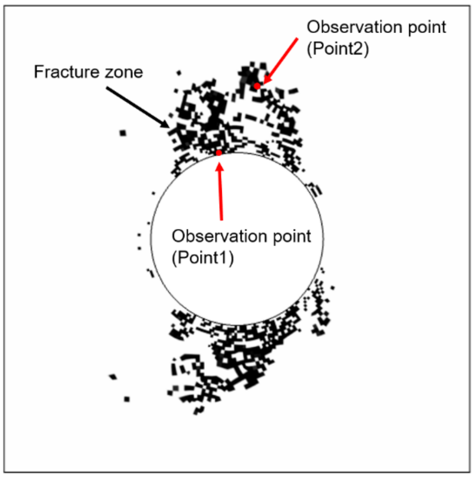

Fig. 16 Setting the observation points. Points 1 and 2 are set in the computed fracture zone where the permeability reduction occurs over time. Point 1 is set in the vicinity of the cavity and Point 2 is set in a place a little away from the cavity.

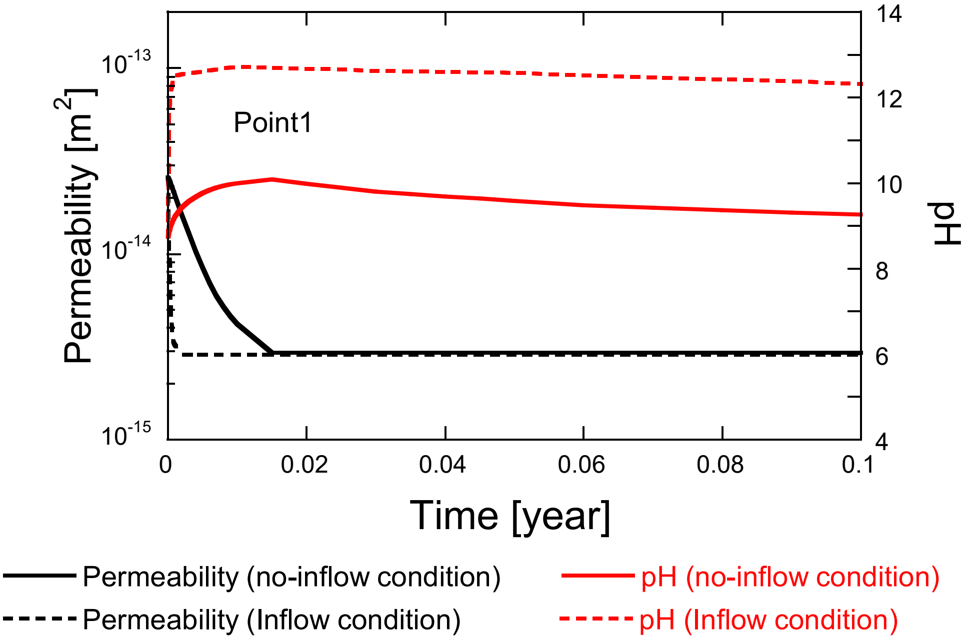

Fig. 17 Changes in permeability and pH within first 0.1 years under no-inflow condition and inflow condition at observation point (Point 1) in fracture zone depicted in **Fig. 16**.

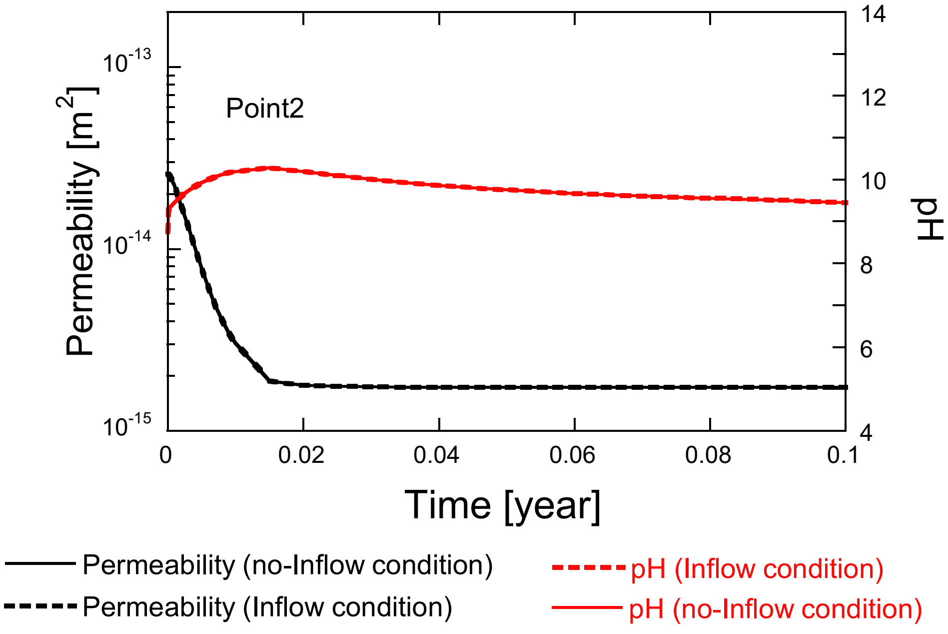

Fig. 18 Changes in permeability and pH within first 0.1 years under no-inflow condition and inflow condition at observation point (Point 2) in fracture zone depicted in **Fig. 16**.

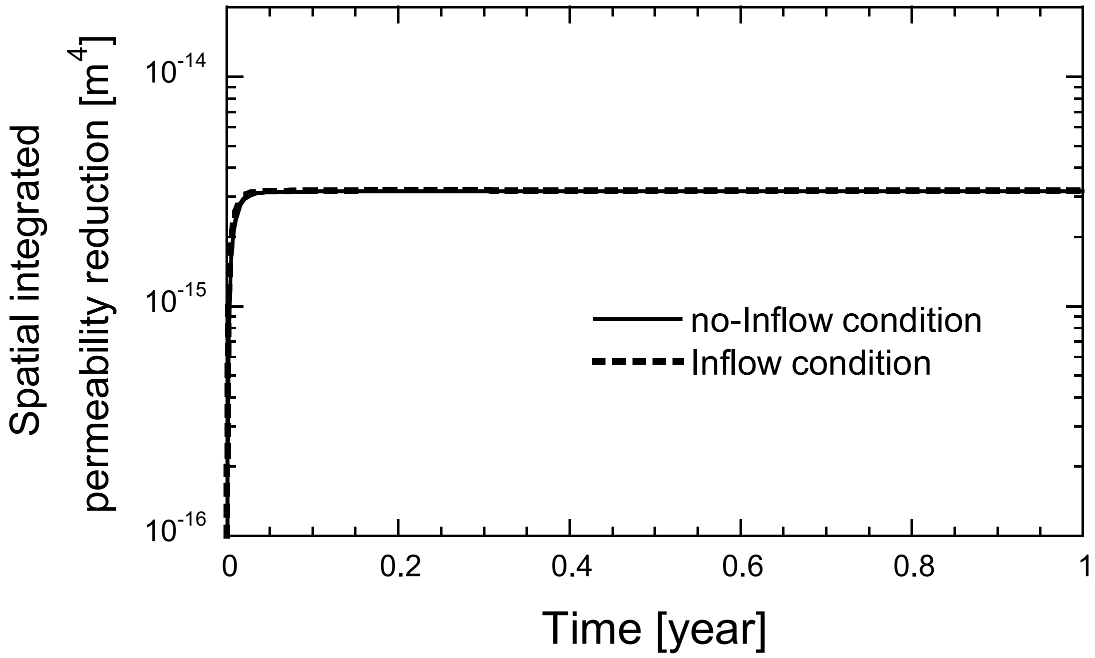

Fig. 19 Changes in space-integrated permeability reduction within 1.0 years under no-inflow condition and inflow condition.

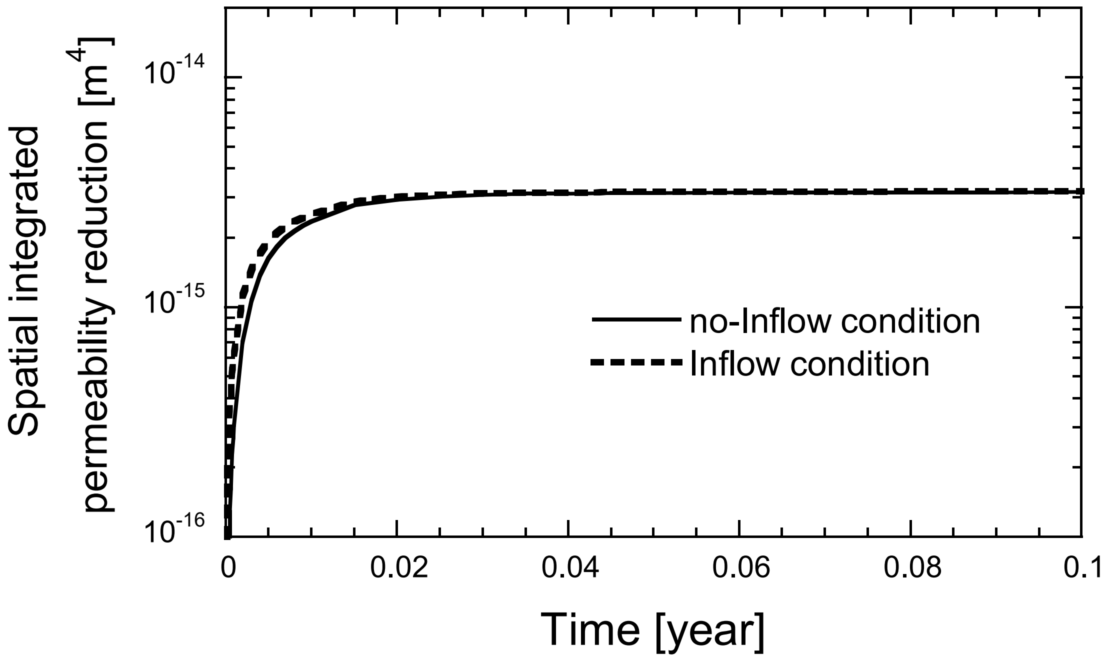

Fig. 20 Changes in space-integrated permeability reduction within first 0.1 years under no-inflow condition and inflow condition.